



# Motion of a deformable droplet in a rectangular, straight channel

Rajarshi Chattopadhyay<sup>1</sup> , Aditya V. Vepa<sup>1</sup> , Gesse Roure<sup>1,2</sup> ,  
Ashish Srivastava<sup>1</sup>  and Robert H. Davis<sup>1</sup> 

<sup>1</sup>Department of Chemical and Biological Engineering, University of Colorado, Boulder, CO 80309-0596, USA

<sup>2</sup>Department of Mechanical and Aerospace Engineering, University of Missouri, Columbia, MO 65201, USA

**Corresponding author:** Robert H. Davis, [robert.davis@colorado.edu](mailto:robert.davis@colorado.edu)

(Received 6 September 2024; revised 25 February 2025; accepted 2 March 2025)

---

The motion and deformation of a neutrally buoyant drop in a rectangular channel experiencing a pressure-driven flow at a low Reynolds number has been investigated both experimentally and numerically. A moving-frame boundary-integral algorithm was used to simulate the drop dynamics, with a focus on steady-state drop velocity and deformation. Results are presented for drops of varying undeformed diameters relative to channel height ( $D/H$ ), drop-to-bulk viscosity ratio ( $\lambda$ ), capillary number ( $Ca$ , ratio of deforming viscous forces to shape-preserving interfacial tension) and initial position in the channel in a parameter space larger than considered previously. The general trend shows that the drop steady-state velocity decreases with increasing drop diameter and viscosity ratio but increases with increasing  $Ca$ . An opposite trend is seen for drops with small viscosity ratio, however, where the steady-state velocity increases with increasing  $D/H$  and can exceed the maximum background flow velocity. Experimental results verify theoretical predictions. A deformable drop with a size comparable to the channel height when placed off centre migrates towards the centreline and attains a steady state there. In general, a drop with a low viscosity ratio and high capillary number experiences faster cross-stream migration. With increasing aspect ratio, there is a competition between the effect of reduced wall interactions and lower maximum channel centreline velocity at fixed average velocity, with the former helping drops attain higher steady-state velocities at low aspect ratios, but the latter takes over at aspect ratios above approximately 1.5.

**Key words:** drops, boundary integral methods, microfluidics

---

## 1. Introduction

The motion of deformable droplets suspended in another fluid is relevant to several application areas, including lab-on-a-chip devices, droplet sorting (Xi *et al.* 2017), micro-reactors (Song *et al.* 2003; Tice *et al.* 2003) and transport of cells (Shields IV *et al.* 2015; Autebert *et al.* 2012; Shen *et al.* 2019). As drop microfluidic (Baroud *et al.* 2010; Anna 2016; Shang *et al.* 2017; Ding *et al.* 2020) applications become more advanced, it is crucial to have a fundamental understanding of the physics behind droplet motion in confined domains to design such systems effectively. Microfluidic systems usually have low Reynolds number, owing to their small dimensions or high fluid viscosity, leading to dominant viscous effects. An early analytical approach to study the motion of a suspended particle or droplet at a low Reynolds number involves the method of reflections, as discussed by Happel & Brenner (1983). Shapira & Haber (1988) studied the motion of small droplets between two stationary plates, investigating the pressure distribution and drag force exerted on the drop using the method of reflections. However, this approach is feasible only when the particle/droplet is considerably smaller than the channel cross-section and far away from the walls, else the method requires multiple reflections with very involved algebra. An alternative, numerical approach commonly used is the boundary-integral method.

The boundary-integral (BI) method, described by Rallison & Acrivos (1978), requires solving a system of integral equations over the channel and particle/drop boundaries, reducing the need for discretising the whole volume to discretising just the boundaries. Zhou and Pozrikidis first used the BI method to dynamically simulate a suspension of two-dimensional, viscous, deformable droplets between two plane parallel walls for Couette and Poiseuille flow (Zhou & Pozrikidis 1993*a,b*, 1994). They found that homoviscous drops (drop-to-bulk viscosity ratio of unity) starting off centre migrate towards the channel centreplane whereas, for a viscosity ratio of 10, the drop migrates either towards the centreplane or towards the wall, depending on its initial position. Several other studies have been done on the motion of a single two-dimensional drop in confined flow (Martinez & Udell 1990; Khayat *et al.* 1997). Coulliette & Pozrikidis (1998) first simulated a fully three-dimensional drop in a circular tube using the BI method. In this study, they observed that the drop migrates toward the centreline in all cases. Griggs *et al.* (2007) conducted a detailed systematic study of the motion of a deformable, three-dimensional drop between two plane parallel walls at low Reynolds number using the BI method, including the effect of various drop sizes, drop-to-bulk viscosity ratios, capillary numbers and initial positions. They observed a decrease in drop velocity with increase in drop size, proximity to walls and viscosity ratio. Their study was built upon the framework offered by several advanced computational techniques developed by Zinchenko *et al.* (1997, 1999) and Zinchenko & Davis (2000) for simulating interaction between deformable droplets, and by Staben *et al.* (2003) for studying the motion of rigid particles in a Poiseuille flow. The BI method has also been used to study drop deformation in a confined shear flow between parallel plates and compared with experiments where oscillatory drop shapes were observed at large capillary numbers and high confinements, and drops retracted to a steady state after stretching at low capillary number (Janssen & Anderson 2007; Vananroye *et al.* 2008; Sibillo *et al.* 2006). Other than straight channels with plane parallel walls and circular tubes, the BI method has also been used to investigate droplet/particle dynamics in T-shaped microchannels (Navarro *et al.* 2020), constricted channel geometries (Navarro *et al.* 2021) such as converging-diverging channels (Kadivar 2018), complex-shaped microchannels (Roure *et al.* 2023, 2024), as well as drop squeezing through smooth obstacles of arbitrary shape (Gissinger *et al.* 2021*b*). In all of the above studies, gravitational/buoyancy forces were neglected.

Another approach for simulating deformable drops and bubbles is the front-tracking method. Unverdi & Tryggvason (1992) used this method for studying single and interacting bubbles and drops. This approach allows solving of the whole Navier–Stokes equation at a non-zero Reynolds number. The lateral migration of a three-dimensional (3-D), deformable, neutrally buoyant drop in a 2-D Poiseuille flow at non-zero Reynolds number was studied by Mortazavi & Tryggvason (2000) using the front-tracking method. They solved the full Navier–Stokes equations and examined the dependence of drop migration on deformation, drop-to-bulk viscosity ratio and Reynolds number. The results obtained using this method are primarily for moderate Reynolds numbers, and hence direct comparison with the BI method is not possible. An interesting behaviour predicted in the work of Mortazavi & Tryggvason (2000) is the cross-stream migration of a drop towards the channel centreplane for low-viscosity drops, whereas migration towards the walls occurred for viscosity-matching drops when a drop was initially placed off centre at non-zero Reynolds number. Hadikhani *et al.* (2018), in their experiments, observed an off-centre equilibrium position of bubbles in a rectangular channel due to a combination of deformation induced and inertial migration, where the bubbles moved closer to the wall with increasing Reynolds number. In the Stokes-flow regime, a deformable drop in a channel with its size comparable to the confinement always moves towards the channel centreplane (Griggs *et al.* 2007), whereas small confined droplets or drops in an unbounded quadratic flow move towards the centreplane in all cases except at drop-to-bulk viscosity ratios between 0.5 and 10, as shown analytically (Chan & Leal 1979), experimentally (Hur *et al.* 2011) and numerically (Cappello *et al.* 2023).

Recently, another approach, called the two-phase lattice-Boltzmann method, was used by Horwitz *et al.* (2014) to simulate a 3-D drop in a 3-D microchannel of a square cross-section, with an emphasis on transient drop deformation with varying non-zero Reynolds number. Upon increasing the Reynolds number, they observed an oscillating drop shape in addition to the formation of a highly unstable cavity region with high interfacial curvature in the trailing edge of the droplet. The lattice-Boltzmann method has also been used to model hydrodynamic squeezing and breakup of droplets in T-junctions (De Menech *et al.* 2008; Chen & Deng 2017). Lan & Khismatullin (2012) studied the lateral migration and deformation of Newtonian liquid drops and leukocytes in a 3-D channel of rectangular cross-section at non-zero Reynolds number using the volume-of-fluid (VOF) algorithm. They explored the possibility of cell cytometry based on the specific lateral equilibrium positions of deformable drops or cells. The VOF algorithm has also been widely used to simulate two-phase flows in T-junction or Y-junction channels with rectangular cross-section (Sarrazin *et al.* 2008; Cherlo *et al.* 2010; Raj *et al.* 2010; Yong *et al.* 2011; Hoang *et al.* 2013a,b; Li *et al.* 2019), and constricted channels with circular cross-section (Singla *et al.* 2024).

Several theoretical works have been performed on the motion of a small spherical droplet/solid particle in a cylindrical tube that provide expressions for force, torque and pressure drop (Greenstein & Happel 1968; Hetsroni *et al.* 1970; Ho & Leal 1975; Olbricht & Leal 1982; Hodges *et al.* 2004). Bretherton (1961) investigated the motion of long bubbles in tubes at the limit of negligible capillary number both analytically and experimentally. Later, Lac & Sherwood (2009) numerically investigated the motion and deformation of a drop along the centreline of a cylindrical tube at a low Reynolds number using the BI method. They studied the effect of drop size relative to tube radius, drop-to-bulk viscosity ratio and capillary number. In addition to drop velocity and deformation, Lac & Sherwood (2009) also studied the additional pressure drop due to the presence of a drop in a cylindrical tube and the film thickness between the drop and the tube walls. They simulated a wider range of capillary numbers than prior work and found a critical

capillary number above which a drop does not reach a steady state but instead experiences continuous deformation. They observed an interesting behaviour for large drops at high capillary numbers and low drop-to-bulk viscosity ratios, where the initial dimple formed at the rear end of a drop slowly evolves into a re-entrant jet, leading to breakup, which was observed in earlier experiments by Olbricht & Kung (1992). Perhaps more surprising, Lac & Sherwood (2009) found that drops with a low viscosity ratio and sufficiently high capillary number move faster than the maximum velocity of the background flow and have increasing steady-state velocity with increasing drop size. This regime has also been observed by Rivero-Rodriguez & Scheid (2018) and Atasi *et al.* (2018) for deformable bubbles in a cylindrical tube studied numerically using a finite-element method and the level-set method, respectively.

Rectangular microchannels have different drop behaviour than circular capillaries because the carrier liquid can bypass the drop through channel corners, potentially altering the flow characteristics. Wang & Dimitrakopoulos (2012) simulated a deformable drop in a microchannel of square cross-section at low Reynolds number using a spectral boundary element method, which was also used by Khan & Wang (2010) to study drop deformation in a confined shear flow. Wang & Dimitrakopoulos (2012) examined the effect of drop size relative to channel height ( $D/H$ , where  $D$  is the drop diameter and  $H$  is the channel height), drop-to-bulk viscosity ratio ( $\lambda$ ) and capillary number ( $Ca$ ) on drop velocity and deformation. They found that larger drops have higher deformation and lower velocities, with the effect being highlighted at higher  $Ca$ , and that the drop velocity decreased with an increase in viscosity ratio for  $\lambda \geq 1$ . They also made a comparison for drop shape and velocity in a circular channel versus a square microchannel with one particular value for each of drop size and capillary number. Wong *et al.* (1995) determined a relation for the pressure drop needed to drive long bubbles in channels of polygonal cross-sections at low capillary numbers. Following that, Rao & Wong (2018) recently modelled the motion of long drops in rectangular channels at small capillary number. In this limit, the long drop has two end caps connected by a long cylinder and is separated by thin films from the microchannel wall. They focused on the carrier-fluid and drop-fluid pressure gradient, and the apparent contact-line drag.

Jakiela *et al.* (2011) did a systematic experimental study of drop velocity in a square channel and its dependence on  $\lambda$ ,  $Ca$  and drop size. Their study was limited to low  $Ca$  ( $10^{-4}$ – $10^{-2}$ ), large drops ( $D > H$ ) and intermediate to large values of  $\lambda$ . They found a strong dependence of drop velocity on both  $\lambda$  and drop size, whereas a strong dependence on  $Ca$  occurred for  $\lambda \sim 1$  but not for  $\lambda < 1$  or  $\lambda \gg 1$ . With the recent developments in lab-on-chip devices for droplet microfluidics, experimental studies have also been done to measure the hydrodynamic resistance of droplets (Vanapalli *et al.* 2009; Jovanović *et al.* 2011; Jakiela 2016) and to investigate their internal flow fields using particle image velocimetry (Kinoshita *et al.* 2007) in both tubes and rectangular channels. Further, experimental studies have been done on long drops at low  $Ca$  to study their curvature at the end caps, pressure drop and velocity relative to the bulk flow in tubes (Zadeh *et al.* 2022) or channels (Helmers *et al.* 2019*b,a*). All of these mentioned experimental studies are limited to large drops ( $D/H > 1$ ) and small capillary numbers  $Ca \lesssim 10^{-2}$ , and none observed a drop moving faster than the maximum background flow velocity in a rectangular channel.

While the studies discussed above represent considerable progress towards understanding the motion of drops in tubes and channels at small or moderate Reynolds numbers, there remains important unexplored physics. In particular, there is a need for a systematic study of the motion of deformable drops in rectangular channels in the Stokes-flow regime consisting of theoretical results for a broad range of parameter values as well as experimental verification, especially for smaller drops ( $D/H \lesssim 1$ ) and larger

capillary numbers ( $Ca \gtrsim 0.1$ ). Thus, the primary aim of the current work is to employ an efficient and accurate 3-D BI method for the motion of a neutrally buoyant, deformable drop in a 3-D microchannel of rectangular cross-section, encompassing various drop sizes, capillary numbers, drop-to-medium viscosity ratios and channel aspect ratios, and then compare the simulation results with experiments. This work has partial overlap with the numerical studies by Wang & Dimitrakopoulos (2012) and Horwitz *et al.* (2014). However, the results of Wang & Dimitrakopoulos (2012) are limited to low capillary numbers ( $Ca < 0.15$ ) and high viscosity ratios ( $\lambda > 0.5$ ), whereas the most interesting phenomena were observed for a cylindrical tube at high capillary numbers and low viscosity ratios by Lac & Sherwood (2009). On the other hand, Horwitz *et al.* (2014) mostly focused on the transient deformation of a drop in a 3-D microchannel of a square cross-section at a non-zero Reynolds number, whereas our focus is more on steady-state drop behaviour in the Stokes-flow regime. Furthermore, there are no studies that investigate the effect of aspect ratio on the drop dynamics in a channel of rectangular cross-sections or that directly compare low-Reynolds-number simulations of the drop dynamics in a straight, rectangular channel with experimental results, to the best of our knowledge. Thus, the goals of the current work are to investigate broader parameter ranges than in the literature, including various channel aspect ratios, compare simulations and experiments over more limited parameter ranges and determine if the interesting physics (drops moving faster than the maximum undisturbed flow velocity, and the velocity of low-viscosity drops increasing with drop size) observed by Lac & Sherwood (2009) for tubes also occurs for channels.

In the current work, we consider a deformable drop in a 3-D channel by using the computational framework implemented by Roure *et al.* (2023) for simulating droplet behaviour in complex-shaped microchannels of finite width in their work. The algorithm uses a moving-frame, boundary-integral (MFBI) method, which was further developed for finite-depth channels by including dynamical meshing of the front and back panels of the channel rather than just the top and bottom plane parallel walls that have been widely used in most prior works. Experiments were performed to observe drop motion and deformation in a macroscopic channel using a highly viscous carrier fluid. In this paper, we first briefly introduce the BI equations and the moving-frame (MF) approach in § 2, followed by a description of the experimental set-up and apparatus in § 3. Next, we provide the theoretical and experimental results including the effect of viscosity ratio, capillary number and channel aspect ratio in § 4, followed by concluding remarks in § 5.

## 2. Boundary-integral formulation

We consider a neutrally buoyant, deformable drop suspended in a flow confined by a 3-D, straight channel of rectangular cross-section. The drop fluid and the suspending medium are both assumed to be Newtonian and surfactant free with fluid viscosities  $\mu_d$  and  $\mu_e$ , respectively. The Reynolds number is assumed very small compared with unity, so the Stokes equations apply. The objective is to study the drop motion and deformation in the microchannel with variations in several important parameters. To this end, a MFBI method was used in this work, which was first introduced by Zinchenko *et al.* (2012) for the motion of a particle in a 2-D microchannel of complex shape but infinite width, then extended by Roure *et al.* (2023) for drops in 3-D channels of finite width.

### 2.1. A moving-frame approach

In the MFBI approach, a computational cell is dynamically constructed around the drop centroid. Since the velocity perturbations caused by a freely suspended drop in a background flow decay rapidly with distance, the cell is constructed around the drop such

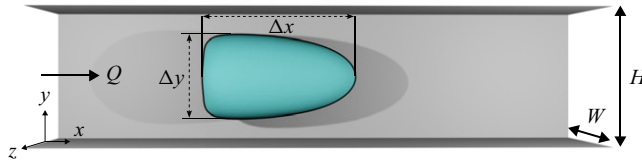


Figure 1. A deformable drop moving in a straight 3-D rectangular channel. Here,  $H$  is the channel height,  $W$  is the channel width and  $Q$  is the flow rate of the suspending medium;  $\Delta x$  and  $\Delta y$  are the length of the drop in the  $x$  and  $y$  directions, respectively.

that the effect of the drop on the flow velocity is negligible at the cell boundary; thus, the velocity on the cell boundary is given by the external flow in the absence of a drop. The MF must be much larger than the drop (approximately three times the drop length is sufficient (Zinchenko *et al.* 2012)) but is still much smaller than the overall channel length.

A 3-D rectangular channel of uniform cross-section is shown in figure 1. The channel has a height  $H$  between its top and bottom panels and a depth (or width)  $W$  between its front and back panels fixed at  $z = \pm W/2$ . The maximum drop lengths in the  $x$ ,  $y$  and  $z$  directions are  $\Delta x$ ,  $\Delta y$  and  $\Delta z$  (not shown in figure 1), respectively. We have adopted the numerical framework by Roure *et al.* (2023) in this paper to simulate 3-D, straight microchannels of rectangular cross-sections. The MF contour is generally obtained from the intersection of a square constructed around the drop centroid (with sides parallel to the  $x$  and  $y$  axes) and the channel profile in the  $z$ -plane. This dynamically constructed square is then extended in  $z$ -direction such that it covers the entire channel depth and hence also includes the front and back panels. Since the drops are usually not much smaller than the channel depth, it is not beneficial to crop the MF in the  $z$ -direction (rather than using the whole channel depth) (Roure *et al.* 2023). The MF approach substantially decreases the computational load for calculating the wall–drop interface interactions, with augmented benefits for drops of size much smaller than the channel.

### 2.2. Boundary-integral equations for velocity of drop interface

The fluid velocity ( $\mathbf{u}$ ) on the drop surface ( $S_d$ ) is calculated using the following BI equation, as derived in Navarro *et al.* (2020). The problem is made dimensionless using the channel height,  $H$ , as the length scale, and the average velocity of the undisturbed flow,  $U_{av} \equiv |Q|/(HW)$  (where  $Q$  is the volumetric flow rate), as the characteristic velocity scale, yielding

$$\mathbf{u}(\mathbf{y}) = \frac{2}{\lambda + 1} \left[ \mathbf{u}_\infty(\mathbf{y}) + 2 \int_{S_\infty} \mathbf{n}(\mathbf{x}) \cdot \boldsymbol{\tau}(\mathbf{x} - \mathbf{y}) \cdot \mathbf{q}(\mathbf{x}) \, dS_x + \mathbf{F}(\mathbf{y}) \right] + 2 \left( \frac{\lambda - 1}{\lambda + 1} \right) \int_{S_d} \mathbf{n}(\mathbf{x}) \cdot \boldsymbol{\tau}(\mathbf{x} - \mathbf{y}) \cdot \mathbf{u}(\mathbf{x}) \, dS_x, \quad (2.1)$$

for  $\mathbf{y} \in S_d$  (drop surface) and

$$\mathbf{q}(\mathbf{y}) = -2 \int_{S_\infty} \mathbf{n}(\mathbf{x}) \cdot \boldsymbol{\tau}(\mathbf{x} - \mathbf{y}) \cdot \mathbf{q}(\mathbf{x}) \, dS_x - \mathbf{F}(\mathbf{y}) - (\lambda - 1) \int_{S_d} \mathbf{n}(\mathbf{x}) \cdot \boldsymbol{\tau}(\mathbf{x} - \mathbf{y}) \cdot \mathbf{u}(\mathbf{x}) \, dS_x - \frac{\mathbf{n}(\mathbf{y})}{|S_\infty|} \int_{S_\infty} \mathbf{n}(\mathbf{x}) \cdot \mathbf{q}(\mathbf{x}) \, dS_x, \quad (2.2)$$

for  $\mathbf{y} \in S_\infty$  (MF surface). The inhomogeneous term  $\mathbf{F}(\mathbf{y})$  in the above equations is given by

$$\mathbf{F}(\mathbf{y}) = \frac{2}{Ca} \int_{S_d} \kappa(\mathbf{x}) \mathbf{G}(\mathbf{x} - \mathbf{y}) \cdot \mathbf{n}(\mathbf{x}) \, dS_x, \quad (2.3)$$

where  $\mathbf{G}(\mathbf{r}) = -(\mathbf{I}/r + \mathbf{r}\mathbf{r}/r^3)/(8\pi)$  is the free-space Green's function corresponding to the fundamental stresslet,  $\boldsymbol{\tau}(\mathbf{r}) = 3\mathbf{r}\mathbf{r}\mathbf{r}/(4\pi r^5)$ , and  $\mathbf{r} = \mathbf{x} - \mathbf{y}$  with  $r = |\mathbf{r}|$ . Here,  $Ca = \mu_e U_{av}/\sigma$  is the capillary number representing the relative strength of viscous stresses compared with interfacial tension. In the above equations,  $\lambda = \mu_d/\mu_e$  is the viscosity ratio between the drop fluid and the suspending fluid,  $\sigma$  is the interfacial tension and  $\kappa$  is the local mean surface curvature at  $\mathbf{x}$  (Zinchenko & Davis 2000). Detailed derivations of (2.1) and (2.2) can be found in Navarro *et al.* (2020). The parameter  $\mathbf{u}_\infty(\mathbf{y})$  in (2.1) is the background flow velocity. In the present case involving flow in a straight channel, we are not required to solve for the background flow using the BI equations for flow inside the channel (as would be necessary for a more general channel geometry); rather, it can be directly calculated for all locations in the channel using the equations for a fully developed, pressure-driven flow in a channel with a rectangular cross-section given by Boussinesq (1868), from which the velocity  $\mathbf{u}_\infty = u_\infty \mathbf{e}_y$  is given by

$$u_\infty = \frac{GH^2}{\mu_e} \left[ \frac{y}{2H} \left( 1 - \frac{y}{H} \right) - 4 \sum_{k=1}^{\infty} \frac{\cosh(\beta_k z) \sin(\beta_k y)}{(H\beta_k)^3 \cosh(\beta_k W/2)} \right], \quad (2.4)$$

where  $\mu_e$  is the suspending fluid viscosity,  $\beta_k = (2k - 1)\pi/H$  and  $G$  is the pressure gradient. The flow rate  $Q$  is related to the pressure gradient by

$$Q = \frac{GH^4}{\mu_e} \left[ \frac{W}{12H} - 16 \sum_{j=1}^{\infty} \frac{\cosh(\beta_j W) - 1}{(H\beta_j)^5 \sinh(\beta_j W)} \right]. \quad (2.5)$$

The above equations are solved simultaneously on the discretised drop surface and MF boundaries using biconjugate-gradient iterations for the resulting system of linear equations. The drop surface discretisation is done using an icosahedron/dodecahedron-based triangulation approach on an initially spherical drop of radius  $a$ , as described in Zinchenko *et al.* (1997), and the mean curvature ( $\kappa$ ) and outward normal ( $\mathbf{n}(\mathbf{x})$ ) on the drop surface are calculated using the best-paraboloid-spline method explained in Zinchenko & Davis (2000). Most of the simulations in this work have been performed with a resolution of 8640 triangular elements on the drop surface, which has been shown to be sufficient for convergent simulations in previous works by Staben *et al.* (2003) and Zinchenko *et al.* (1997). Time is made dimensionless as  $t^* = t/(H/U_{av})$ . Time stepping in the simulations uses  $\Delta t^* \sim \mathcal{O}(Ca \delta_x)$ , where  $\delta_x$  is the minimum node-to-node distance on the drop mesh and  $Ca$  is the capillary number. Once the velocity of the drop interface is found at a given time step, the nodes on the drop surface are advanced using a first-order Euler's scheme, which usually results in good accuracy, provided sufficiently high resolution is used on the drop surface (and, hence, small time steps).

### 3. Experimental methods

#### 3.1. Experimental set-up

The set-up for performing experiments on the motion of a suspended drop in a straight rectangular channel is shown in figure 2. It consists of three main components: a syringe pump, a flow cell and a camera. The first component is a NE-4000 two-channel syringe pump that is used to modulate the flow rate of the continuous fluid. Changing the flow rate changes the average flow velocity in the channel and hence lets us accurately control the capillary number. The syringe pump was calibrated by weighing the fluid collected versus time, with further refinement by employing tracer drops. The second component is a flow cell manufactured by machining acrylic (the transparent nature of acrylic allows easy

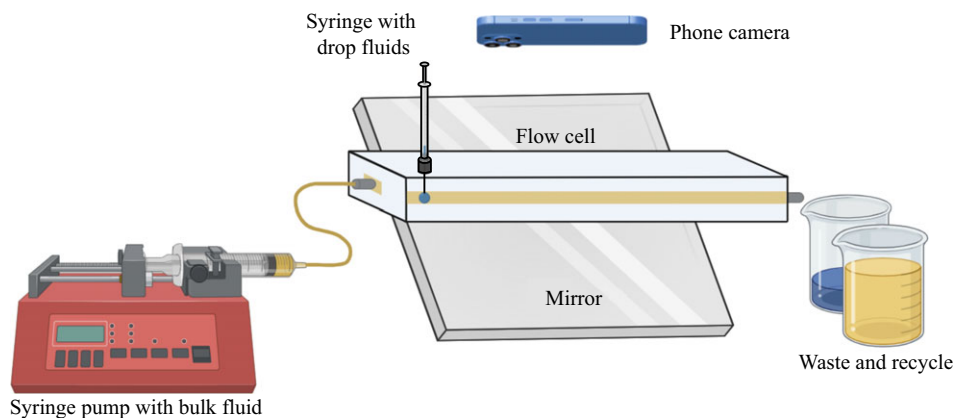


Figure 2. Schematic of the experimental set-up consisting of a syringe pump for controlling flow rate, a flow cell for the droplet and the suspending medium, a syringe for inserting a drop and a camera for recording drop motion. A mirror allows the drop to be viewed from the side as well as top.

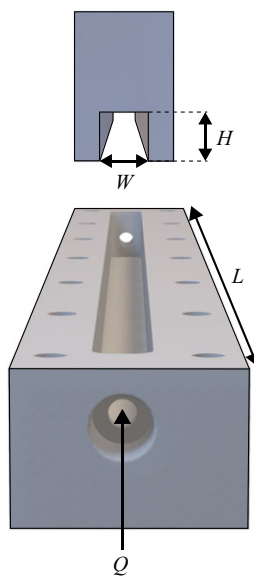


Figure 3. The flow cell and a sample insert that would be fitted into the flow cell cavity. The direction of flow into the cell is shown via  $Q$ .

visualisation) at the University of Colorado Boulder Chemical and Biological Engineering Instrument Shop. The flow cell has a cavity of dimensions 29.3 cm in length, 10.1 mm in height and 15.3 mm in width, within which inserts of different geometries were fitted to control the aspect ratio of the straight channel, as shown in figure 3. The macroscopic flow cell facilitates easy drop visualisation without the need for an expensive microscope set-up. Viscous fluids were employed to yield small Reynolds numbers. The viscous suspending fluid results in moderate capillary numbers within the range of 0.1–1. In contrast, aqueous systems typically have smaller capillary numbers, unless the interfacial tension is very small, due to smaller viscosity and the accompanying velocity required for small Reynolds number. Two inserts were designed (using AUTOCAD) and manufactured by machining acrylic for these experiments: a square channel (cross-section  $5 \times 5$  mm) and a rectangular

channel with an aspect ratio of 2:1 (cross-section  $5 \times 10$  mm). Once the insert was placed in the flow cell, the entire cavity was sealed via a screwed-on acrylic plate, which also includes a rubber gasket to avoid fluid leaking outside the confines of the channel insert. Droplets were inserted into the flow cell with a syringe through an opening on the side of the flow cell (figure 2) while the carrier fluid was at rest. This opening has a septum to seal off the inside of the flow cell and avoid bubble formation during needle insertion/extraction. A syringe-holder attachment was also designed and 3D-printed to dispense consistent, specific drop volumes and to ensure the drop's initial position is close to the centreline within the straight channel. Once the drop was inserted into the flow cell and the syringe pump turned on, the drop travelled along the length of the flow cell. To verify the consistency of the pump flow, a small tracer drop (diameter approximately 10 times smaller than the channel height) positioned close to the channel centreline was used in the experiments in addition to the primary drop. The tracer drop was placed several diameters away from the primary drop such that its hydrodynamic contributions to the motion of the primary drop were negligible. Measuring the velocity of the tracer drop allowed us to measure the centreline velocity and verify that the pump was working without significant fluctuations. The tracer drop velocities were reproducible within 3%–4% variation. This variation may arise from a slightly off-centred position of the tracer drop or minor pump fluctuations.

The third component is the camera, which is an iPhone 13 Pro. Videos were recorded at a full HD resolution ( $1920 \times 1080$  pixels) and 60 frames per second. The videos were later analysed to extract important droplet information, such as droplet deformation and velocity using the trackmate plugin of ImageJ, which outputs the temporal variation of drop position as well as deformation. The position vs time data were split into 10 equal regions while the drop was moving, and velocity was calculated from each of these regions. In all cases, the drop velocity showed very little variation beyond the entrance region. Therefore, position vs time data from beyond that region were used for determining the steady-state velocity ( $U_s$ ) of the droplet by fitting a straight line to the data and calculating the slope. This velocity value was subsequently made non-dimensional by dividing with the average velocity of the bulk fluid in the channel ( $U_{av}$ ) or the maximum flow velocity at the channel centreline ( $U_{max}$ ). A mirror was placed at  $45^\circ$  underneath the flow cell such that it provided a side view of the flow cell that could be seen via the camera. This allowed us to confirm that the drop did not settle/drag against the bottom of the channel insert and stayed centred throughout its movement along the channel. The macroscopic nature of this experimental set-up allows the use of a common phone camera, and hence easy accessibility to understanding microfluidic droplet phenomena.

### 3.2. *Fluid and flow properties*

There are three main fluids used in the current work: two droplet-phase fluids and one bulk-phase fluid. Castor oil obtained from Nature's Oil Bulk Apothecary was used as the bulk-phase fluid because of its high viscosity. The droplet-phase fluids are 8% (volume) aqueous glycerol solution (acquired from Macron Fine chemicals), and silicon oil (polydimethylsiloxane (PDMS) acquired from MicroLubrol). These fluids were chosen due to their differing viscosities and close densities to the bulk castor oil. Near-neutral buoyancy between the drop phase and the bulk phase is important to avoid significant sedimentation of the droplet. Each drop was dyed (food colouring dye consisting of water, glycerine, FD&C blue, citric acid and sodium benzoate was used for aqueous glycerol drops and a benzyl-benzoate-based dye was used for the PDMS drops) to ensure a high visual contrast between the droplet and the castor oil. The kinematic viscosity ( $\nu$ ) of each

<b>Bulk fluid</b>	$\rho_e$ [g cm <sup>-3</sup> ]	$\mu_e$ [g cm <sup>-1</sup> s <sup>-1</sup> ]	<b>Drop fluid</b>	$\rho_d$ [g cm <sup>-3</sup> ]	$\mu_d$ [g cm <sup>-1</sup> s <sup>-1</sup> ]	$\lambda = \mu_d/\mu_e$ [-]	$\sigma$ [mN m <sup>-1</sup> ]
Castor oil	0.956	11.6	8 % aq. glycerol	1.024	0.0122	0.001	17.4 ± 1.0
Castor oil	0.956	11.6	PDMS	0.969	9.69	0.838	5.0 ± 0.8

Table 1. Characteristic properties of the fluids used in the experiments as drop phase and bulk phase measured at 21 °C.

fluid was measured with a glass capillary viscometer and its density was determined using a hydrometer. The interfacial tension of each drop fluid was measured using the pendant-drop method. A pendant drop of the droplet fluid immersed in the bulk castor oil was videotaped and analysed using the pendant-drop plugin of ImageJ to find the interfacial tension between the droplet and bulk fluids. The plugin utilises the Young Laplace equation, where the pressure at equilibrium at each point along the drop interface is related to the curvature at that point by a constant interfacial tension. The measured properties of the fluids are listed in table 1. The uncertainty associated with the interfacial tension measurements recorded in table 1 is the standard deviation of 7 trials for each case.

### 3.3. Experimental parameters

A wide range of experimental conditions was used. The drop dynamics was studied by varying the drop size, drop-fluid viscosity, the flow rate of the bulk fluid and the channel aspect ratio. The value of  $D/H$  (spherical drop diameter/channel height) was varied in a range of 0.2–0.92 by controlling the drop volumes dispensed. As shown in table 1, two different viscosity ratios ( $\lambda$ ), 0.838 and 0.001, were considered in this work. The capillary number ( $Ca = \mu_e U_{av}/\sigma$ ) which is a measure of viscous force relative to interfacial tension force, was varied in a range of 0.2–0.8 by changing the bulk fluid flow rate and hence the average velocity of the background flow ( $U_{av}$ ). A channel Reynolds number is defined for the experiments as  $Re_c = \rho_e U_{av} H/\mu_e$ , based on the density ( $\rho_e$ ) and viscosity ( $\mu_e$ ) of the external bulk fluid, the average flow velocity of the channel ( $U_{av}$ ) and channel height ( $H$ ). The range of channel Reynolds number is 0.003–0.014, with each of the limits corresponding to extremes of flow rates required for achieving the above-mentioned range of capillary numbers. The temperatures recorded while doing the experiments were within a range of 21.2–21.9 °C. Finally, the aspect ratio was varied between a square channel and a rectangular (2 : 1) channel by using different acrylic inserts. Each condition was run for multiple trials (greater than 5) to allow a suitably low confidence interval. In the following section, the effect of changes in the above parameters on drop behaviour is shown both computationally and experimentally.

## 4. Results

In the numerical results presented here, the drops are initially spherical and centred in the cross-section of a square microchannel, unless stated otherwise (see § 4.3 for the effect of varying aspect ratio). The drop velocity,  $U$ , is defined as the fluid velocity averaged over the drop volume:

$$U = \frac{1}{V} \int_V \mathbf{u}(\mathbf{x}) dV. \tag{4.1}$$

Once released at or near the centreline of the micro-channel, the droplet moves along the channel and its shape deforms. Starting from an initial spherical shape, the front region

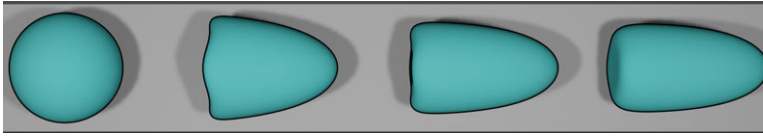


Figure 4. Numerical results of a drop at different times with  $D/H = 0.4$ ,  $Ca = 0.6$  and  $\lambda = 0.4$  gradually reaching a steady state.

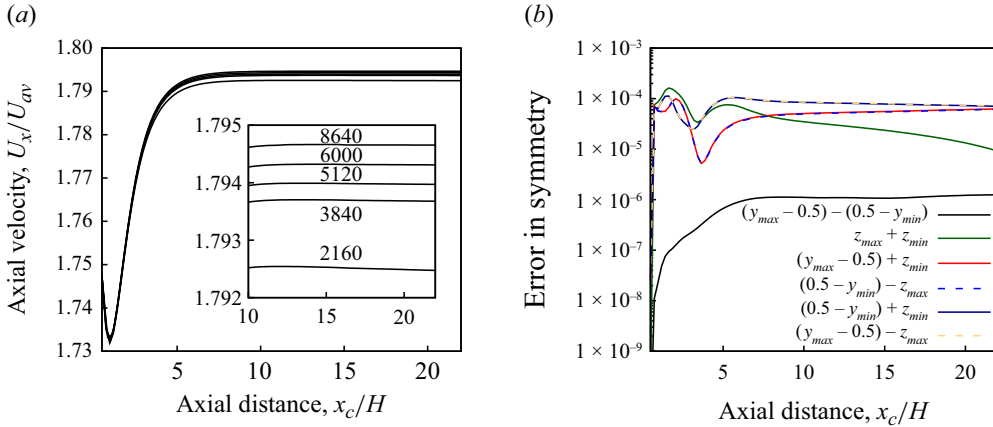


Figure 5. (a) Drop velocity with increasing number of triangular elements on the drop surface from 2160 to 8640 (bottom to top) for a drop of  $D/H = 0.7$ ,  $\lambda = 1$ ,  $Ca = 0.5$ . (b) Testing the symmetry of a steady drop of  $D/H = 0.7$ ,  $\lambda = 1$ ,  $Ca = 0.5$  with 8640 surface triangles by comparing its top ( $y_{max}$ ), bottom ( $y_{min}$ ), front ( $z_{max}$ ) and back ( $z_{min}$ ) positions.

of the droplet becomes pointed while the rear flattens (see figure 4), which results in a transient response of the drop velocity, eventually reaching a bullet-shaped steady state.

Although the accuracy of this algorithm has been tested in a prior work by Roure *et al.* (2023), we performed further tests for the current geometry. Figure 5(a) shows the volume-averaged velocity of a drop with  $D/H = 0.7$ ,  $\lambda = 1$ ,  $Ca = 0.5$  translating in a straight channel under a pressure-driven flow, with varying number of triangles used to discretise the drop surface. The difference in the velocities of the drop gradually decreases with increasing number of triangles, with the relative difference in steady velocities of order  $10^{-3}$  between 2160 and 8640 triangles and of order  $10^{-4}$  between 6000 and 8640 triangles, justifying our choice of 8640 triangles. In our algorithm, we simulate the drop without using the channel symmetry. The nodes on the surface of the triangles, although initially symmetrically distributed, later become asymmetric as the drop deforms. Therefore, comparing the top, bottom, front and back positions of the drop shape provides another test of accuracy. In figure 5(b), we compare the top ( $y_{max}$ ), bottom ( $y_{min}$ ), front ( $z_{max}$ ) and back ( $z_{min}$ ) extremities of a drop of  $D/H = 0.7$ ,  $\lambda = 1$ ,  $Ca = 0.5$  with respect to the channel centreline ( $y = 0.5$ ,  $z = 0$ ). Note that  $y \in [0, 1]$  and  $z \in [-0.5, 0.5]$ . It is evident that in all cases the error in their position with respect to the centreline is less than  $10^{-4}$ , which is approximately 100 times smaller than the edge of a mesh triangle, thereby demonstrating high accuracy of our algorithm.

In the following sections, we show some transient results but primarily focus on the non-dimensional steady-state drop velocity ( $U_s/U_{av}$ ) and steady-state drop deformation ( $D_T$ ), where  $U_s$  is the dimensional steady-state drop velocity, and  $D_T = \Delta x/\Delta y$  is the ratio of the length of the deformable drop in the axial direction ( $\Delta x$ ) to its length in the transverse direction ( $\Delta y$ ). Simulations are shown for a wide range of parameters and compared with

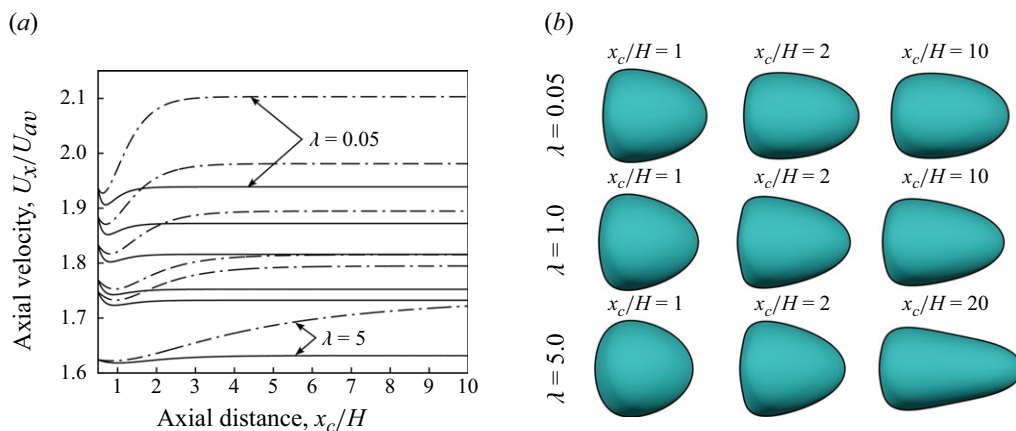


Figure 6. (a) Evolution of drop velocity in the axial direction with distance traversed for a droplet of size  $D/H = 0.7$ . The solid lines are for  $Ca = 0.2$  with  $\lambda = 0.05, 0.2, 0.4, 0.8, 1, 5$  (top to bottom) and the dot-dash curves are for  $Ca = 0.5$  with  $\lambda = 0.05, 0.2, 0.4, 0.8, 1, 5$  (top to bottom). (b) Side view of drop shapes at different centroid positions ( $x_c/H$ ) along the channel while approaching steady state for  $Ca = 0.5, D/H = 0.7$  at  $\lambda = 0.05, 1, 5$  (top to bottom).

experiments for a more limited range. Experimental results are only shown for steady-state drop velocity and deformation, since the transient drop behaviour is sensitive to drop initial position and shape, which are difficult to reproducibly control. Fortunately, deformable, neutrally buoyant drops of size comparable to the channel height always migrate to the channel centre at low Reynolds number (Chan & Leal 1979; Griggs *et al.* 2007; Cappello *et al.* 2023) so that the steady-state results do not depend on the initial conditions.

#### 4.1. Effect of viscosity ratio and drop size

First, we investigate the effect of changes in drop-to-bulk viscosity ratio on drop velocity. Figure 6(a) shows the transient evolution of dimensionless drop axial velocity ( $U_x/U_{av}$ ) with distance moved by drop centroid ( $x_c/H$ ) along the channel. The drop velocity first decreases due to the initial deformation, which results in increased resistance to flow, until a minimum is reached, then it starts increasing as the drop becomes more streamlined until it reaches a steady state. The steady velocity is reached after the drop has travelled a few drop diameters, in most cases. We also see from figure 6(a) that the drop steady-state velocity decreases with increasing viscosity ratio, as a higher viscosity ratio means higher viscous drag, higher shear stress in the fluid film between the drop and the walls and reduced internal flow, and hence a lower drop velocity. A more viscous drop also travels a longer distance before reaching a steady state; a drop with  $Ca = 0.5$  and  $\lambda = 5$  does not reach a steady state within the span of figure 6(a). This particular drop travelled approximately 40 channel heights before reaching a steady state. The high viscosity ratio coupled with a high capillary number ensures a dominant viscous force and slow deformation. Note that the solution by Boussinesq (1868) gives  $U_{max}/U_{av} = 2.096$  for the undisturbed velocity at the centre of a square channel, which is close to the steady-state velocity of the least viscous drop ( $\lambda = 0.05$ ) with  $D/H = 0.7$  at the higher capillary number ( $Ca = 0.5$ ). Figure 6(b) shows a side view of the transient shape of a 3-D, deforming drop as it travels along the channel for different viscosity ratios. A higher viscosity ratio results in higher deformation at steady state, although it takes longer for a high-viscosity drop to reach a steady state due to increased hydrodynamic resistance.

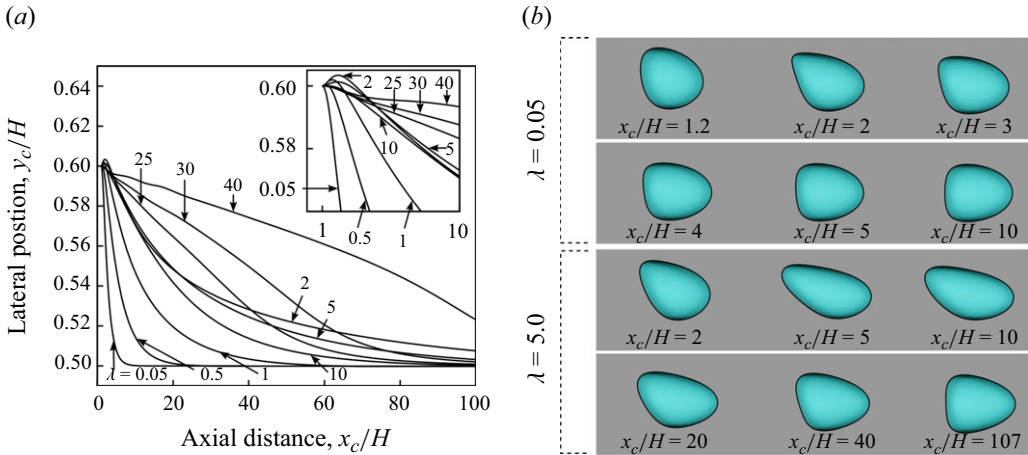


Figure 7. (a) Cross-stream migration of drop centroid position (solid lines) with distance travelled along the channel for  $\lambda = 0.05, 0.5, 1, 2, 5, 10, 25, 30, 40, D/H = 0.6, Ca = 0.5$  and initial lateral position  $y_c/H = 0.6$ . (b) Drop shape at different positions along the channel length while migrating laterally for  $\lambda = 0.05$  and 5 from (a).

A deformable drop placed away from the centreline of a channel undergoes cross-streamline migration due to its deformed, non-spherical shape. Figure 7(a) shows the centroid position of a drop of size  $D/H = 0.6$  that was placed off centre initially at  $y_c/H = 0.6$  for different values of viscosity ratio at a fixed capillary number. The drop migrates towards the channel centreline in all cases. A drop of lower viscosity ratio migrates cross-stream faster than one of higher viscosity ratio in the range of  $\lambda \in [0.05, 1]$ , due to the slower deformation and larger hydrodynamic resistance of the latter. A similar trend is observed for large viscosity ratios ( $\lambda > 25$ ) due to reduced internal flow. However, a non-monotonic behaviour is observed in cross-stream migration for  $\lambda \in [2, 25]$ . Figure 7(b) shows the deformed drop shapes while undergoing lateral migration for a low and high  $\lambda$ . Initially, the drop starts elongating along the flow profile and migrating away from the top wall. Tail formation is evident due to the drop interaction with the nearby top wall. As the drop travels along the channel length and approaches the centreline, its shape becomes more compact and symmetric, eventually reaching a steady shape. Generally, a higher-viscosity drop attains a steady state with higher deformation, and since the phenomenon of cross-stream migration is attributed to drop deformation, it might be counter-intuitive to observe that a high-viscosity drop has a slower cross-stream migration velocity, as can be seen in figure 8(a) for short times. Even though the final steady-state deformation is lower in a low-viscosity drop, the drop deforms faster in the initial stages due to reduced hydrodynamic resistance. This phenomenon is shown in figure 8(b), where the transient tip-to-tip maximum drop length non-dimensionalised by drop diameter ( $l/D$ ) is plotted for different viscosity ratios. This maximum tip-to-tip drop length ( $l/D$ ) is the maximum distance between two points on the drop surface (in any direction) and is a better metric for cross-stream migration where both the lateral drop length ( $\Delta y$ ) and the axial drop length ( $\Delta x$ ) are important. The low-viscosity drops reach their maximum deformation faster, which allows them to attain high cross-stream velocities rapidly, immediately after release. However, high-viscosity drops experience greater deformation in the long run, helping them maintain a higher cross-stream migration velocity longer. Due to this competition, we see a non-monotonic behaviour in the intermediate viscosity

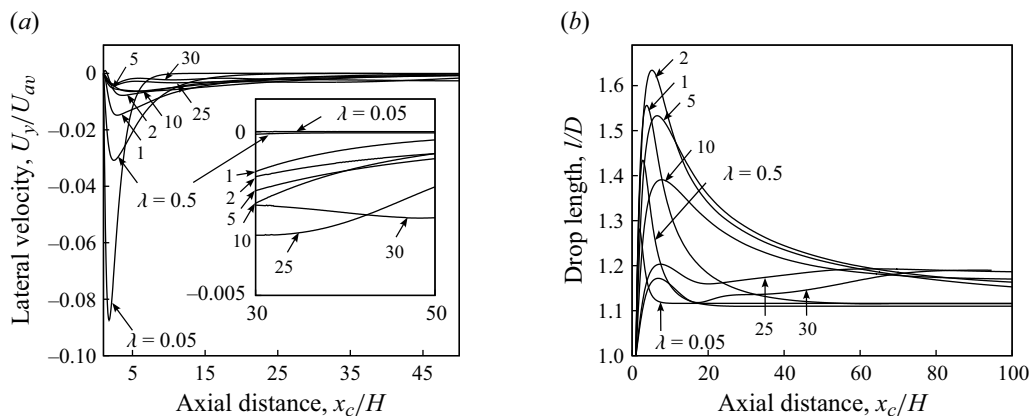


Figure 8. (a) Transient cross-stream migration velocity ( $U_y$ ) and (b) deformation in the axial direction of a drop for  $\lambda = 0.05, 0.5, 1, 2, 5, 10, 25, 30, D/H = 0.6, Ca = 0.5$  and initial lateral position  $y_c/H = 0.6$ .

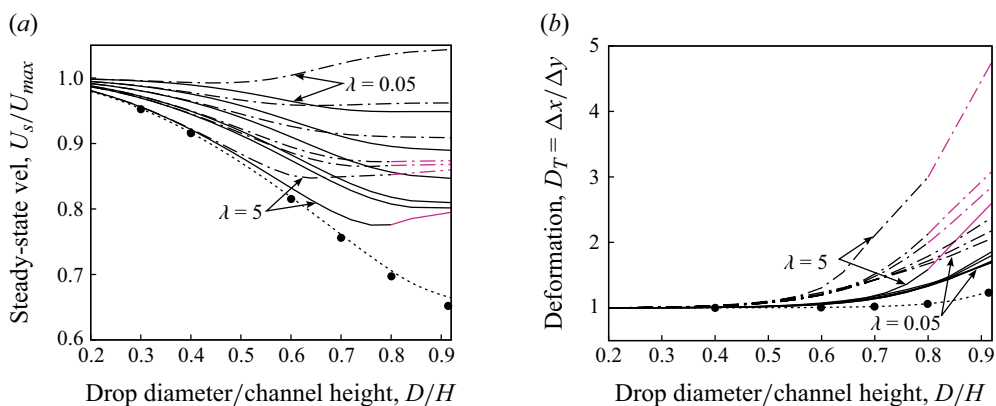


Figure 9. Change in steady-state (a) drop velocity and (b) deformation with increasing drop size and  $\lambda = 0.05, 0.2, 0.4, 0.8, 1, 5$  (top to bottom for (a) and bottom to top at large  $D/H$  for (b)) for  $Ca = 0.3$  (solid), and  $Ca = 0.6$  (dot-dash). The magenta portion of the curves were initially started as a prolate ellipsoid instead of a sphere. The dotted line in (a) and (b) are for drops with  $Ca = 0.1, \lambda = 10$  and the filled circle points (●) are numerical data from Wang & Dimitrakopoulos (2012) at the same conditions.

ratio values ( $\lambda \in [2, 25]$ ). A similar trend was observed by Griggs *et al.* (2007) in their work involving the motion of a drop between parallel walls.

Figures 9(a) and 9(b) show curves for the change in drop steady-state velocity and deformation with drop diameter for different values of drop-to-bulk viscosity ratio ( $\lambda$ ), respectively. The special case  $Ca = 0.1$  and  $\lambda = 10$  is included to show good agreement between the BI simulations done in this work and the simulations done by Wang & Dimitrakopoulos (2012) using a spectral-boundary-element method. The velocity decreases with increasing drop size in all cases except  $\lambda = 0.05$  with  $Ca = 0.6$  (discussed later). A larger drop has increased interaction with the channel walls, and spans across both fast and slow streamlines which make the drop slower. As in figure 6(a), we see a decreasing steady-state drop velocity with increasing viscosity ratio ( $\lambda$ ) in figure 9(a). Figure 9(b) shows that, for large drop diameters, a more viscous drop undergoes greater deformation since they experience a larger shear stress. For a fixed capillary number, the drop deformation for small drop sizes ( $D/H < 0.6$ ) is not significant, and almost

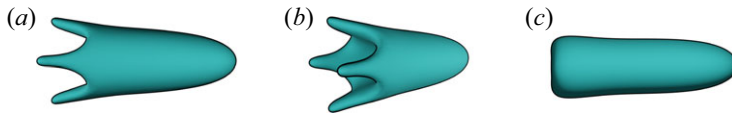


Figure 10. Highly deformed, unstable four-tailed drops prior to satellite drop pinch-off at a  $Ca = 0.6$ ,  $\lambda = 1$  and  $D/H = 0.92$ . Panel (a) shows a side view of the drop and in (b) we see a perspective from which all the four tails are visible. (c) Steady-state shape of the same drop when simulated with an initial prolate ellipsoid shape.

independent of the drop-to-bulk viscosity ratio ( $\lambda$ ). Size effects are more prominent for larger drops ( $D/H > 0.7$ ) at higher capillary number ( $Ca$ ) values.

Drops with relatively high  $\lambda$  or high  $Ca$  in figure 9 start experiencing unstable tail formation beyond a certain drop diameter ( $D/H \gtrsim 0.8$ ) when initially started as a sphere. As noted previously, a drop with a higher drop-to-bulk viscosity ratio undergoes larger deformation before reaching a steady state. A higher viscosity ratio coupled with a high capillary number, and greater wall interactions for larger drops, yields large deformation and formation of a four-tailed structure for sufficiently large drops, as shown in figures 10(a) and 10(b). Such drops seldom reach a steady state, and their tails eventually become narrow, leading to pinch off of very small satellite drops. Interestingly, we found that, if a drop is started as a prolate ellipsoid instead of a sphere, such that its minor axis is smaller than the sphere's radius and therefore is further away from the walls initially, then the simulations could be continued successfully until a steady state is reached without tail formation (figure 10c), and this part of the curve is coloured magenta in figure 9. Lac & Sherwood (2009) also reported a critical capillary number in their work on drop motion in a cylindrical microchannel, above which a drop does not reach a steady state but instead undergoes continued deformation. Since the focus of the current study is steady-state drop velocities, we did not include pinch-off nor continued simulations after the formation of satellite drops.

Tail pinch-off is not limited to high viscosity ratios. We observed similar behaviour in large drops for low viscosity ratios at high capillary numbers. Figure 11 shows one such simulation where a drop with  $D/H = 0.92$ ,  $\lambda = 0.1$  and  $Ca = 0.8$  displays satellite drop pinch-off of its tails. The drop deforms gradually and initially forms a dimple in its posterior, which turns into a re-entering jet-like intrusion. Eventually, its tails become increasingly narrow, leading to pinch-off. Lac & Sherwood (2009) observed a similar re-entering jet in their simulations with a low-viscosity drop in a cylindrical tube at a high capillary number. Since cylindrical tubes are radially symmetric, tail formation is not seen in that channel geometry, rather Lac & Sherwood (2009) observed breakup of low-viscosity drops when the re-entrant jet reached the tip of the drop. This phenomenon was also observed experimentally in a cylindrical tube by Olbricht & Kung (1992). More recently, Nath *et al.* (2017) performed an extensive numerical study on droplet breakup in a cylindrical channel using a coupled level-set and VOF method focusing on the effect of drop size, capillary number and viscosity ratio. They observed several outcomes based on these parameters, where a drop either forms a long tail or a re-entering jet and breaks up into small daughter or satellite droplets, which sometimes coalesced back to a single drop further down the channel.

One of the most interesting results of this work is the increase in steady-state velocity with increasing drop diameter for large  $Ca$  and small  $\lambda$ , such as observed in figure 9(a) for  $Ca = 0.6$  and  $\lambda = 0.05$  and (to a lesser extent)  $\lambda = 0.2$ , as typically we would expect a larger drop to be slowed down due to wall interactions. When  $\lambda < 1$ , the drop fluid has a lower viscosity than the suspending fluid, which, generally, makes it easier to drive the flow. A possible explanation is provided by considering the roles of form drag and friction

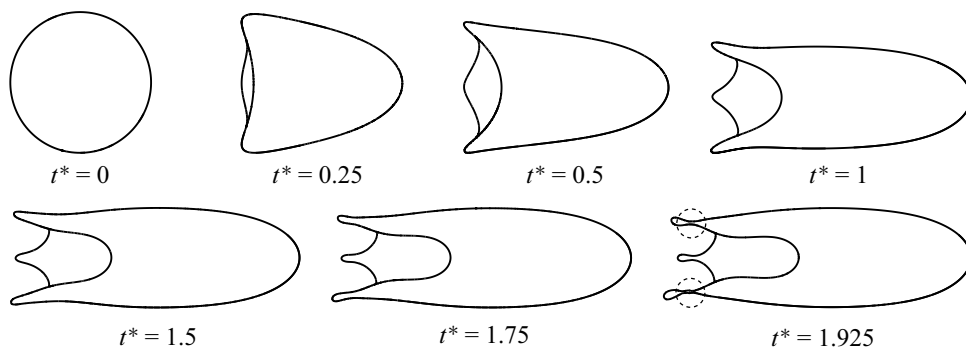


Figure 11. Cross-section of transient shapes of a drop of undeformed diameter  $D/H = 0.92$  with  $\lambda = 0.1$  and  $Ca = 0.8$ , developing a dimple that eventually becomes a re-entrant jet and finally leads to tail pinch-off (dashed circles) at  $t^* = 1.925$ .

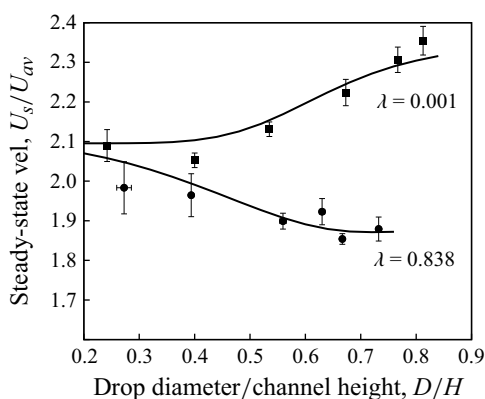


Figure 12. Comparison between numerical (curves) and experimental (points) results for steady-state drop velocity with increasing drop diameter for  $\lambda = 0.001$  (aqueous glycerol drop), and  $0.838$  (PDMS drops) at  $Ca = 0.74$ . The squares ( $\blacksquare$ ) and circles ( $\bullet$ ) are experimental data for  $\lambda = 0.001$  and  $\lambda = 0.838$ , respectively, with error bars representing 90 % confidence intervals from repeated experiments.

drag. Form drag is due to pressure and increases with the increasing cross-sectional area of the drop perpendicular to the flow direction, whereas friction drag is due to viscous shear stresses and increases with surface area parallel to the flow direction. These two contributions are comparable for spherical particles and viscous drops, but the form drag will be reduced and the friction drag will be increased if a drop becomes elongated. This deformation typically leads to a net increase in drag or a reduction in drop velocity. However, for low-viscosity drops, form drag dominates and so a net decrease in drag or increase in drop velocity can occur if the drop deformation is substantial (large  $Ca$ ). This phenomenon is discussed further in § 4.2.

Figure 12 shows a comparison between experimental and simulation results for steady-state drop velocity versus drop diameter at a fixed capillary number ( $Ca = 0.74$ ) and two different viscosity ratios,  $\lambda = 0.001$  and  $\lambda = 0.838$ . The lower and the higher viscosity ratios correspond to 8 % aqueous glycerol drops and silicon oil drops, respectively, suspended in castor oil (table 1). There is good agreement between the experiments and simulations, where the theory lies within the 90 % confidence intervals of the experimental results for all cases except at  $D/H = 0.27$  for the lower curve at  $\lambda = 0.838$ ,  $Ca = 0.74$ .

Previous studies have shown that small drops below a certain critical  $D/H$  (depending on  $\lambda$  and  $Ca$ ) and with a viscosity ratio within a specified range ( $\lambda \in [0.5, 10]$  for drops in an unbounded flow (Chan & Leal 1979) and  $\lambda \in [0.7, 10]$  for small drops in a tube (Cappello *et al.* 2023)) have a tendency to undergo lateral migration towards the walls if started off centre initially. We suspect that our smallest drop in the curve with  $\lambda = 0.838$  and  $Ca = 0.74$  might have been placed slightly off centre initially in the experiments and slowly migrated further from the centre as it travelled along the channel length, hence resulting in a slower steady-state velocity observed in experiments. In fact, Cappello *et al.* (2023), in their study on the stable, equilibrium, lateral position of drops in a cylindrical microchannel showed that, in the inertialess limit, the critical drop size for lateral migration towards the walls around  $\lambda = 0.8$  is approximately  $D/H = 0.27$ , which might be slightly different for a channel of rectangular cross-section but attests to our suspicion. These experiments verify the predicted trend of an increase in steady-state drop velocity with increasing drop diameter for a low viscosity ratio ( $\lambda = 0.001$ ) and high capillary number ( $Ca = 0.74$ ), whereas the drop velocity decreases with increasing drop size at the larger viscosity ratio.

The maximum flow velocity at the channel centreline for a square channel from the Boussinesq (1868) solution is,  $U_{max}/U_{av} \sim 2.096$ . Another interesting observation in figures 9(a) and 12 is that the drop steady-state velocity increases beyond the maximum flow velocity with drop diameter. Lac & Sherwood (2009) explained this behaviour for a cylindrical channel with an asymptotic analysis assuming the flow of a long, slender drop in a capillary. They considered a long slender drop to be similar to an annular flow of two immiscible fluids, where the inner fluid of viscosity  $\lambda\mu$  occupies a cylinder of radius  $R\delta$  in a capillary of radius  $R$ , and the outer fluid of viscosity  $\mu$  occupies the annular film of thickness  $(1 - \delta)R$ . Assuming the inner cylinder to be a long drop with axial velocity  $V$ , Lac & Sherwood (2009) obtained the following relation between the drop velocity and the average flow velocity in the channel:

$$\frac{V}{U_{av}} = \frac{2\lambda + (1 - 2\lambda)\delta^2}{\lambda + (1 - \lambda)\delta^4}. \quad (4.2)$$

For a pressure-driven flow in a cylindrical channel,  $U_{max}/U_{av} = 2$ , where  $U_{max}$  is the maximum undisturbed flow velocity at the channel centreline. Equation (4.2) reveals that it is possible to attain  $V/U_{av} > 2$  at  $\lambda \lesssim 0.5$  for a range of  $\delta$ . Thus, it is possible for a low-viscosity drop with large deformation to obtain a steady-state velocity that exceeds the maximum velocity of the undisturbed flow. This conclusion is also expected for a rectangular channel, although the analysis would be more complex due to the corners.

#### 4.2. Effect of capillary number

In this section, we further examine the effect of capillary number on the velocity and deformation of a drop. The capillary number is a measure of the relative strength of deforming viscous forces to the restoring interfacial tension forces, so a higher capillary number results in greater deformation. Figure 13 shows simulations of the transient evolution of drop velocity with distance travelled along the channel length. As in figure 6, the drop velocity decreases at first and reaches a minimum, but then starts increasing until it reaches a steady state. Since a higher capillary number is associated with higher deformation, the drop travels a longer distance before it reaches a steady state for higher  $Ca$ . The drop steady-state velocity increases with increasing capillary number ( $Ca$ ). A drop with higher deformation has more of its volume close to the maximum flow velocity at the channel centreline and farther from the walls, which results in a higher

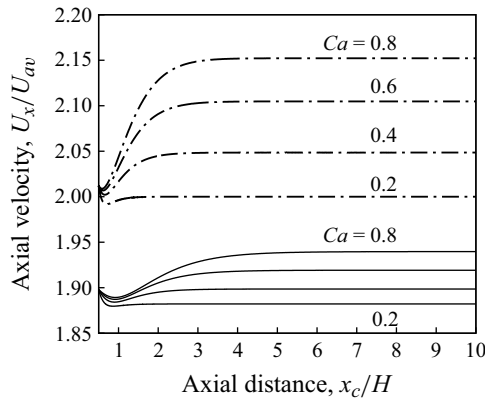


Figure 13. Simulations of the evolution of drop velocity in the axial direction with distance traversed for a droplet of size  $D/H = 0.6$ . The dot-dashed curves are for  $\lambda = 0.05$  with  $Ca = 0.2, 0.4, 0.6, 0.8$  (bottom to top) and the solid curves are for  $\lambda = 0.5$  with  $Ca = 0.2, 0.4, 0.6, 0.8$  (bottom to top).

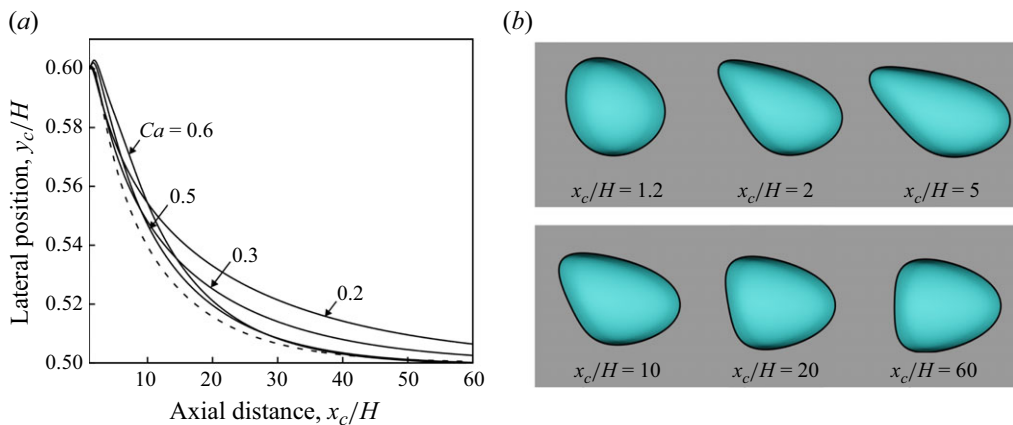


Figure 14. (a) Cross-stream migration of drop centroid position (solid lines) with distance travelled along the channel for  $Ca = 0.2, 0.3, 0.5, 0.6$ ;  $D/H = 0.6$ ;  $\lambda = 1$ ; and initial lateral position  $y_c/H = 0.6$ . The dashed line is for a drop with  $Ca = 0.5$ ,  $\lambda = 1$ ,  $D/H = 0.6$ , and an initial position of  $y_c/H = 0.6$  in a channel of infinite depth using the algorithm of Navarro *et al.* (2020). (b) Drop shape at different positions along the channel length while migrating laterally for  $Ca = 0.5$  corresponding to (a).

drop velocity with increasing  $Ca$ . Figure 13 also shows that more viscous drops have lower velocities and a weaker dependence on  $Ca$ .

As mentioned in § 4.1, a deformable drop placed off centre in a channel for the conditions examined here experiences cross-stream migration towards the centreline. Figure 14(a) shows the transient centroid position of a drop of size  $D/H = 0.6$  that was initially placed off centre at  $y_c/H = 0.6$  for different capillary numbers at a fixed drop-to-bulk viscosity ratio. A drop with a higher capillary number deforms more and hence has a more streamlined shape with a higher velocity expected both parallel and perpendicular to the wall. In figure 14(a), we see that a drop with  $Ca = 0.5$  migrates faster than the ones with  $Ca = 0.2, 0.3$ , and the drop with  $Ca = 0.6$  although it is initially slower than  $Ca = 0.5$ , eventually crosses over at  $x_c/H \approx 30$  and reaches the centreline earliest among the four. This behaviour is because the drop with  $Ca = 0.6$  has the highest deformability and hence forms the longest tail (which makes it slower than the other cases initially due

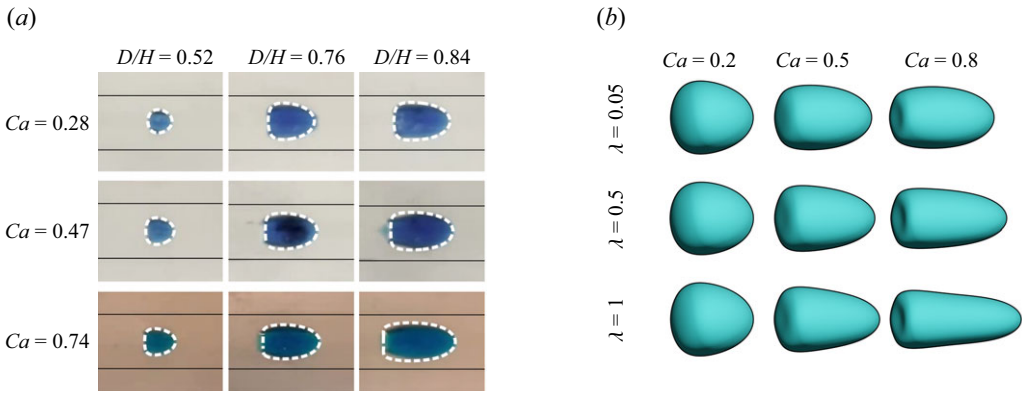


Figure 15. (a) Steady-state shapes of a drop with increasing drop diameter  $D/H = 0.52, 0.76, 0.84$  for  $Ca = 0.28, 0.47, 0.74$  and  $\lambda = 0.001$  obtained from experiments overlaid by outlines for steady-state drop shapes obtained from BI simulations at same conditions. (b) Steady-state shapes of a drop of  $D/H = 0.76$  for  $\lambda = 0.05, 0.5, 1$  with increasing capillary number  $Ca = 0.2, 0.5, 0.8$  from simulations.

to increased interactions with its closest wall), but remains highly deformed for a longer time than the low  $Ca$  drops, helping it maintain a high lateral velocity for longer and hence reaching the centreline earliest. The dashed line in figure 14(a) is for the transient centroid position of a drop with  $Ca = 0.5, \lambda = 1, D/H = 0.6$  and initial lateral position  $y_c/H = 0.6$  in a channel of infinite depth simulated adopting the numerical framework of Navarro *et al.* (2020). The drop migrates slightly faster than the one in a square channel, which can be attributed to the absence of added sidewall interactions in an infinite-depth channel as opposed to a square channel. Figure 14(b) shows the transient deformed drop shapes corresponding to the curve for  $Ca = 0.5$  in the channel of square cross-section in figure 14(a). As in figure 7(b), the drop starts deforming and migrating towards the centreline, forms a tail due to interaction with its closest wall, and then eventually retracts its tail and becomes compact; finally, it reaches a symmetric steady shape at the channel centreline.

Figure 15(a) shows the steady-state shapes of drops of different diameters with increasing capillary number at  $\lambda = 0.001$  as seen in the experiments overlaid by steady-state drop outlines obtained from simulations at the same conditions, showing good agreement. A more elongated drop can be seen with increasing  $Ca$ , due to higher viscous deformation forces. Figure 15(b) shows the steady-state shapes of a drop of size  $D/H = 0.76$  with increasing capillary number for different viscosity ratios. With increasing  $Ca$ , the drop develops a dimple on its backside due to the flow indenting its posterior. The increase in deformation with capillary number is greater for a higher viscosity ratio, since a large  $\lambda$  is also associated with greater viscous forces on the interface. Noticeably, we see a wide rear and a tapered front for the drop at  $\lambda = 1$  and  $Ca = 0.8$ , but for  $\lambda = 0.05$  this shape is no longer exhibited at high capillary numbers. The dimple at the posterior end of the drop with  $\lambda = 0.05$  and  $Ca = 0.8$  evolves into a re-entering jet at higher capillary numbers when the shape-preserving interfacial tension forces are overpowered, as seen in figure 11.

Figure 16 shows the change in steady-state drop velocity and its deformation with drop diameter and capillary number for a bulk-to-drop viscosity ratio of 0.5. As discussed earlier, the steady-state velocity typically decreases with increasing drop size due to increased interaction with the channel walls and lower fluid velocity near the walls, except for cases with very low drop-to-bulk viscosity ratios. In figure 16, both the steady-state velocity and the deformation of the drop increase with increasing capillary number for

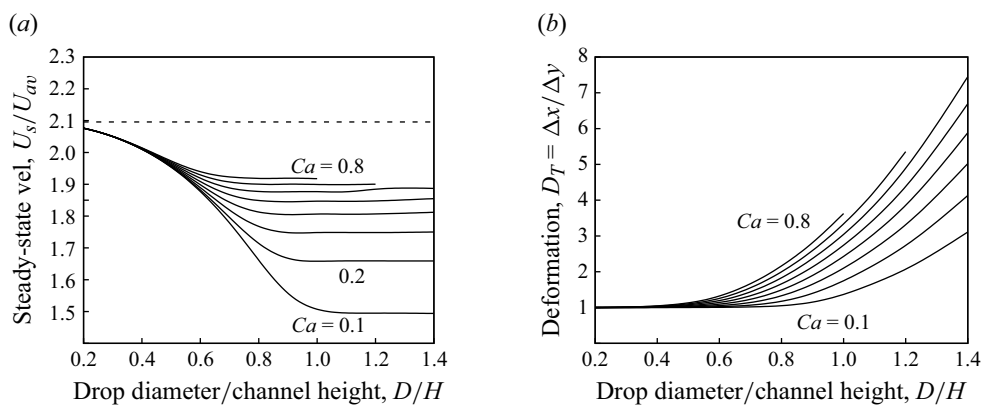


Figure 16. Steady-state (a) drop velocity and (b) drop deformation with increasing drop diameter and  $Ca = 0.1, 0.2, 0.3, 0.4, 0.5, 0.6, 0.7, 0.8$  (bottom to top) at  $\lambda = 0.5$ .

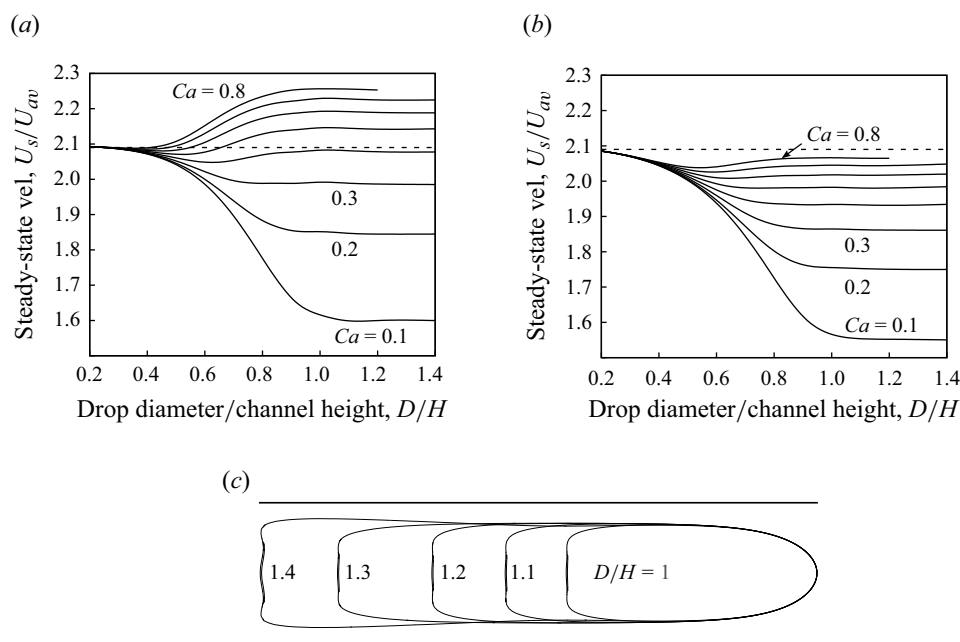


Figure 17. Steady-state drop velocity with increasing drop diameter and  $Ca = 0.1, 0.2, 0.3, 0.4, 0.5, 0.6, 0.7, 0.8$  (bottom to top) at (a)  $\lambda = 0.05$  (b)  $\lambda = 0.2$ . (c) Steady-state shapes of drops with  $\lambda = 0.05$ ,  $Ca = 0.7$  and  $D/H = 1, 1.1, 1.2, 1.3, 1.4$  (left to right).

drops of all sizes. In figure 17(a), for a very low viscosity ratio,  $\lambda = 0.05$ , the steady-state velocity decreases with increasing drop radius for lower capillary numbers, whereas it has an opposite trend for higher capillary numbers. This observation is due to the fact that drops with very low  $\lambda$  but high  $Ca$  experience much less skin friction and hence are able to attain higher velocities, even greater than  $U_{max}$ , as explained in § 4.1, whereas for higher viscosity ratios the steady-state velocity gradually approaches  $U_{max}$  with increasing capillary number, as seen in figures 16(a) and 17(b). Figure 17(b) shows the change in steady-state velocity with drop diameter for increasing  $Ca$  at  $\lambda = 0.2$ . Here, we see that the drops reach a steady state without breaking, with their velocity almost equal to  $U_{max}$  at

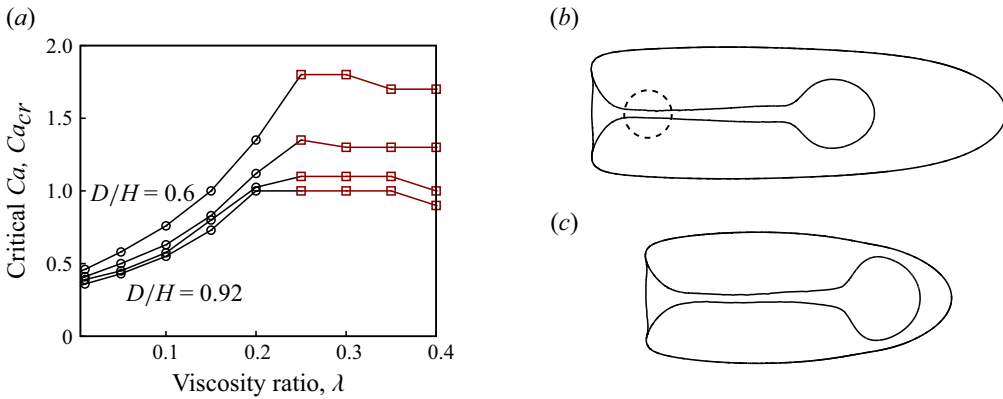


Figure 18. (a) Critical  $Ca$  at which either the steady-state velocity becomes greater than  $U_{max}$  ( $\circ$ ), or the drop breaks ( $\square$ ) with increasing viscosity ratio ( $\lambda$ ) for drops of sizes  $D/H = 0.6, 0.7, 0.8, 0.92$  (top to bottom). Drop breakup when (b) the origin of the re-entrant jet undergoes necking (dashed circle) for a drop with  $D/H = 0.92$ ,  $\lambda = 0.4$ ,  $Ca = 0.9$  or (c) the jet reaches the tip of a drop with  $D/H = 0.8$ ,  $\lambda = 0.25$ ,  $Ca = 1.1$ .

$Ca = 0.8$ , showing little dependence on drop diameter. For a viscosity ratio lower than 0.2, drops at  $Ca = 0.8$  reach a steady state at a higher velocity with increasing drop diameter, attaining faster speeds than  $U_{max}$ . A similar behaviour was found in numerical studies on the motion of a bubble in a cylindrical channel by Rivero-Rodriguez & Scheid (2018) and Atasi *et al.* (2018), where they observed a transition in the change in steady-state bubble velocity from decreasing with increasing bubble size to increasing with increasing bubble size between a  $Ca$  of 0.25 and 0.5. They also observed a steady-state velocity greater than  $U_{max}$  for large bubbles above a critical  $Ca$  in this regime. A larger drop is always found to have a higher deformation for any viscosity ratio due to an increase in the ratio of deforming to restoring forces and higher interaction with the walls. Note that a few curves in figures 16 and 17 for the large capillary numbers are discontinued after a certain drop size because drop breakup was observed due to unstable tail or re-entrant jet formation. Figure 17(c) shows the steady-state shapes of some drops with increasing  $D/H$  for  $\lambda = 0.05$  and  $Ca = 0.7$ .

Figure 18(a) shows the critical capillary number ( $Ca_{cr}$ ) at which the drop steady-state velocity becomes larger than the maximum velocity of the background flow at the channel centreline ( $U_{max}$ ) and how it changes with viscosity ratio for different drop sizes, as obtained from BI simulations. For a square channel,  $U_{max} \sim 2.096$ . In agreement with our previous results,  $Ca_{cr}$  increases with increasing viscosity ratio up to  $\lambda \approx 0.25$ . On the other hand,  $Ca_{cr}$  decreases with increasing drop size owing to the fact that larger drops travel at greater speeds at these low viscosity ratios. A capillary number with drop steady-state velocity greater than  $U_{max}$  was not found beyond  $\lambda = 0.25$  for any of the drop sizes shown in figure 18(a). In these cases, the drops experience breakup beyond a certain  $Ca$ , with values shown using red squares in figure 18(a). A re-entrant jet was observed in all cases, causing breakup in one of the three ways including (i) necking of the origin of the re-entrant jet (figure 18b), (ii) penetration by the jet up to the tip of the drop (figure 18c) or (iii) tail pinch-off before the re-entrant jet is able to penetrate a substantial amount (figure 11).

Figure 19 shows a comparison between experimental and simulation results of steady-state drop velocity and deformation versus drop diameter for a fixed drop-to-bulk viscosity ratio ( $\lambda = 0.001$ , 8% aqueous glycerol drops in castor oil) and three different capillary numbers,  $Ca = 0.28, 0.47$  and  $0.74$ . The capillary number in the experiments was varied by changing the flow rate of the suspending fluid. As shown in table 1, there is an

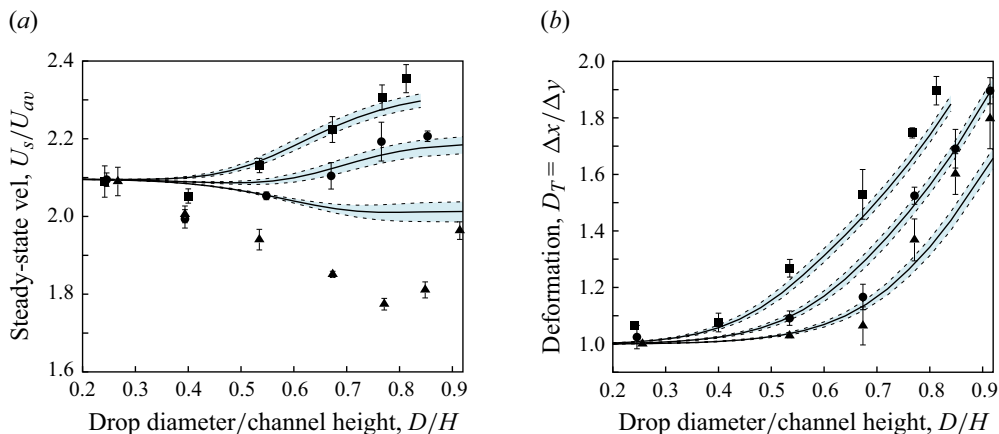


Figure 19. Comparison between numerical (curves) and experimental (symbols) results for (a) steady-state drop velocity and (b) drop deformation with increasing drop diameter. The comparison was done for  $\lambda = 0.001$  (aqueous glycerol drop) at  $Ca = 0.74 \pm 0.06$ ,  $0.47 \pm 0.03$ ,  $0.28 \pm 0.02$ , with the confidence bands representing the uncertainty in capillary number ( $Ca$ ) calculations arising from the standard deviation of interfacial tension ( $\sigma$ ) measurements. Experimental results are provided at  $Ca = 0.74$  (■),  $Ca = 0.47$  (●) and  $Ca = 0.28$  (▲), with the error bars representing 90% confidence intervals.

uncertainty associated with the interfacial tension ( $\sigma$ ) values measured using the pendant-drop method. Naturally, this uncertainty propagates to the calculated values of capillary number, where  $Ca = \mu_e U_{av} / \sigma$ . The confidence bands of the theory curves (solid lines) in figure 19 show the corresponding variation in the simulations. There is a good agreement for  $Ca = 0.74$  and  $Ca = 0.47$  with considerable overlap between theory and experiments in both figures 19(a) and 19(b), but for  $Ca = 0.28$  the measured velocities are 10%–20% below the values predicted by the simulations. We suspect it could be an effect of surfactant in our experiments arising from impurities in the castor oil or the blue inorganic dye used for our 8% aqueous glycerol drops. The presence of surfactants slows down a drop suspended in a plane Poiseuille flow (Pak *et al.* 2014) or a rectangular channel (Luo *et al.* 2018) due to the Marangoni effect. A lower capillary number corresponds to a greater importance of interfacial tension forces and surfactants in the experiments. Moreover, we suspect that, at a low viscosity ratio, there is a more significant effect of surfactants due to reduced interfacial mobility, although further investigation involving the modelling of a surfactant-covered drop in microchannels is required. Atasi *et al.* (2018) observed an approximately 10% decrease in steady-state velocity of nearly spherical bubbles (low  $Ca$ ) due to a small amount of surfactant in their numerical study involving the bubble dynamics in a tube. This result affirms the possible explanation for the disparity observed between experiments and simulations in figure 19(a). Nevertheless, our experimental results display similar behaviour as the simulation results in figure 17, where both the steady-state drop velocity and deformation increase with increasing capillary number, decrease with increasing drop diameter for a low capillary number, but increase with increasing drop diameter for a high  $Ca$ , and the steady-state drop deformation always increases with capillary number. Figures 17(a) and 19(a) also suggest there is a critical capillary number value near  $Ca = 0.4$ , at which this switch in behaviour from the steady-state velocity decreasing with increasing  $D/H$  to increasing with increasing  $D/H$  occurs for  $\lambda \ll 1$ .

Figure 20 shows the steady-state deformed drop height ( $\Delta y/H$ ) with increasing undeformed drop diameter ( $D/H$ ) for different capillary numbers at  $\lambda = 0.05$  and 0.2, obtained from BI simulations. The steady-state deformed drop height is defined here as the transverse length of a deformed drop that has reached steady state non-dimensionalised by

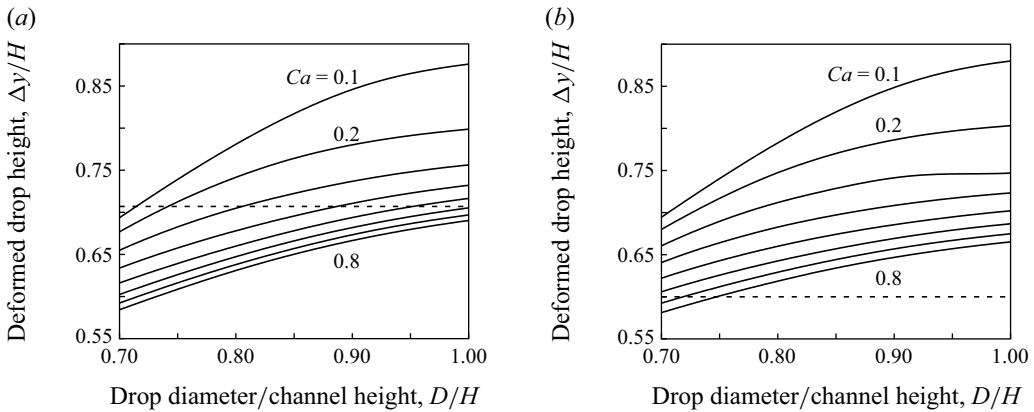


Figure 20. Fraction of channel height that the deformed steady-state drop occupies with increasing drop diameter for  $Ca = 0.1, 0.2, 0.3, 0.4, 0.5, 0.6, 0.7, 0.8$  (top to bottom) at (a)  $\lambda = 0.05$  (solid lines) (b)  $\lambda = 0.2$  (solid lines). The dashed line is at  $\Delta y/H = 0.707$  in (a) and at  $\Delta y/H = 0.6$  in (b), signifying the maximum  $\delta$  at which a slender drop can have a velocity greater than  $U_{max}$  for  $\lambda = 0.05$  and 2, respectively, using (4.2) for tubes. The solid lines are simulations for square channels.

channel height. As discussed previously, slender drops can attain a velocity greater than the maximum flow velocity in the channel at low viscosity ratios. There is a threshold value of steady-state drop height ( $\delta$ ) obtained from (4.2) for tubes, below which a drop can become faster than  $U_{max}$ , and this  $\delta$  increases with decreasing drop-to-bulk viscosity ratio. Therefore, at a fixed viscosity ratio, a drop that is able to survive up to a high enough capillary number to experience enough deformation and reach a steady state with a  $\Delta y/H$  less than this critical value of  $\delta$  obtained from (4.2) will be able to attain a velocity greater than  $U_{max}$ . This critical drop height was found to be  $\delta = 0.707$  at  $\lambda = 0.05$ , and we see from figure 20(a) that drops with higher  $Ca$  have their curves below the dashed line at  $\Delta y/H = 0.707$ . In qualitative agreement with this result, we observe in figure 17(a) that large drops with high  $Ca$  attain a steady-state velocity higher than  $U_{max}$ , and the steady-state velocity increases with increasing drop diameter. The critical drop height below which a drop can go faster than  $U_{max}$  at  $\lambda = 0.2$  was found to be  $\delta = 0.6$  from (4.2). In figure 20(b), we see that the deformed drop height ( $\Delta y/H$ ) obtained from BI simulations at  $\lambda = 0.2$  for different capillary numbers are mostly above  $\Delta y/H = 0.6$ . This again is in qualitative agreement with our observation in figure 17(b), where we see that the steady-state velocity increases with capillary number, slowly approaches  $U_{max}$  and becomes almost equal to  $U_{max}$  at  $Ca = 0.8$ . The authors would like to reiterate that the above comparison is qualitative, since (4.2) was derived by Lac & Sherwood (2009) for long drops in a cylindrical channel whereas the present study involves a channel of rectangular cross-section and drops of size comparable to the channel height.

### 4.3. Effect of aspect ratio

The aspect ratio of a rectangular channel has a significant effect on the steady-state velocity of the drop. In the present finite-depth channel simulations, we specify the volumetric flow rates  $Q$  and use the corresponding Boussinesq solution for the flow in a rectangular duct as the undisturbed flow in the absence of a drop. The most straightforward way to compare finite-depth simulations of rectangular channels with different aspect ratios is to keep a fixed  $Q/W$ , where the channel width,  $W$ , is varied to change the aspect ratio. In this manner, we can match the average flow velocities,  $U_{av}$ , between simulations with different aspect ratios.

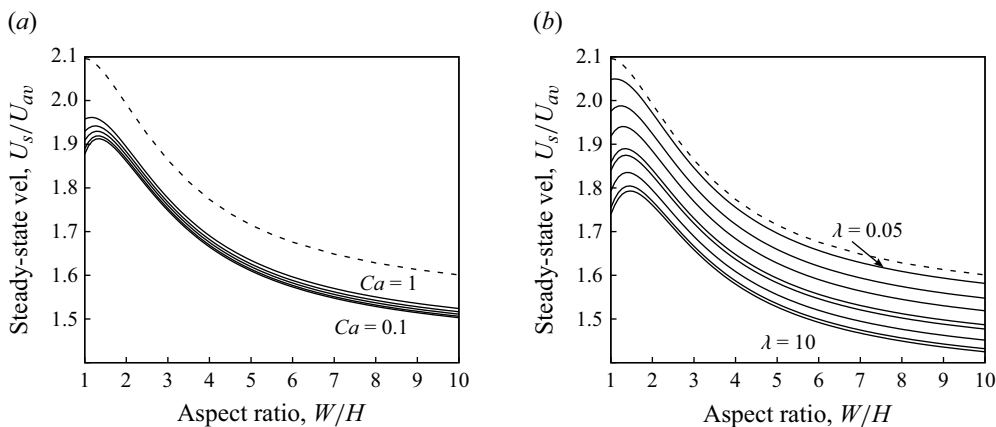


Figure 21. (a) Steady-state drop velocity (solid lines) with increasing aspect ratio for  $Ca = 0.1, 0.3, 0.5, 0.7, 1.0$  (bottom to top),  $\lambda = 0.5$  and  $D/H = 0.6$ . (b) Steady-state drop velocity (solid lines) with increasing aspect ratio for  $\lambda = 0.05, 0.2, 0.4, 0.8, 1, 2, 5, 10$  (top to bottom),  $Ca = 0.4$  and  $D/H = 0.6$ . The dashed line shows the values for  $U_{max}/U_{av}$  from the Boussinesq (1868) solution for a rectangular channel.

Figure 21 shows the effect of aspect ratio on the steady-state velocity of a drop non-dimensionalised by the average velocity of the background flow. In figures 21(a) and 21(b), simulation results for drop steady-state velocity with increasing aspect ratio are shown for different values of capillary number and drop-to-bulk viscosity ratio, respectively. In both cases, the drop steady-state velocity first increases slightly up to an aspect ratio of approximately 1.3, and then decreases monotonically with increasing aspect ratio. For the Boussinesq (1868) solution, the channel maximum velocity (centreline velocity) of the background flow decreases with increasing  $W/H$  and fixed  $Q/W$ , from  $U_{max}/U_{av} = 2.096$  for a square cross-section ( $W/H = 1$ ) and asymptotes to 1.5 as  $W/H \rightarrow \infty$ , which is the case of Poiseuille flow between plane parallel walls. Due to this decrease in the channel maximum velocity with increasing aspect ratio, the steady-state drop velocity also decreases. However, for increasing aspect ratios in the approximate range  $1 < W/H < 2$ , there is a competition between the effect of decreasing interaction with the walls, which helps a drop attain higher steady-state velocity, and a lower channel maximum velocity, which results in lower steady-state velocity. The net result is a maximum in each curve near  $W/H = 1.3$ , except for a viscosity ratio of 0.05 (figure 21b, top curve). As discussed in §§ 4.1 and 4.2, a higher steady-state velocity is observed in figure 21(b) with a decreasing viscosity ratio ( $\lambda$ ) due to lower viscous drag, and a lower steady-state velocity is observed with decreasing capillary number ( $Ca$ ) in figure 21(a) due to less deformation of the drops leading to a lower percentage of its volume experiencing the maximum flow velocity near channel centreline. However, the dependence on capillary number is weaker than the dependence on viscosity ratio.

In figure 22, the variation in steady-state drop deformation with increasing aspect ratio is shown for different capillary numbers (figure 22a) and drop-to-bulk viscosity ratios (figure 22b). Two different parameters have been used to describe the change in deformation with aspect ratio: (i) deformation along channel height,  $D_{T,y} = \Delta x/\Delta y$ , and (ii) deformation along channel width,  $D_{T,z} = \Delta x/\Delta z$ . The aspect ratio of the channel is changed by keeping the height ( $H$ ) constant and increasing the channel width ( $W$ ). Figures 22(a) and 22(b) show that both  $D_{T,y}$  and  $D_{T,z}$  decrease with increasing aspect ratio due to decreased wall interaction. Again,  $D_{T,z}$  decreases more than does  $D_{T,y}$  due to the channel width increasing with the aspect ratio. There is a modest effect of

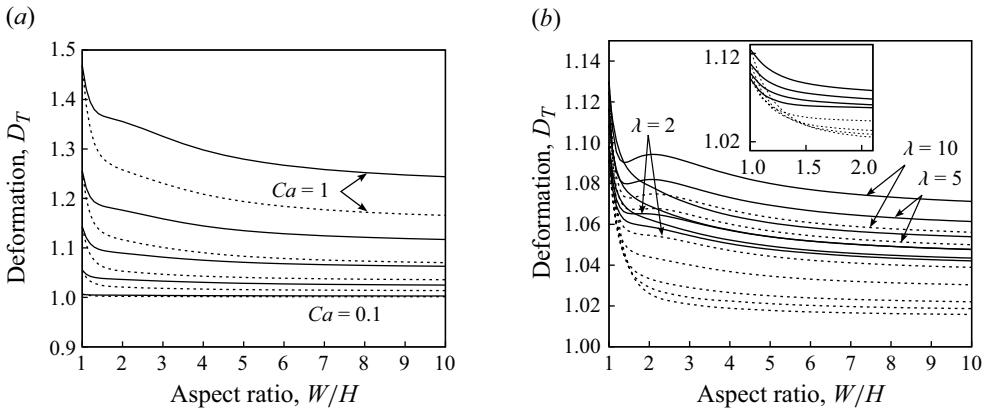


Figure 22. (a) Steady-state drop deformation with increasing aspect ratio for  $Ca = 0.1, 0.3, 0.5, 0.7, 1.0$  (bottom to top),  $\lambda = 0.5$  and  $D/H = 0.6$ . (b) Steady-state drop deformation with increasing aspect ratio for  $\lambda = 0.05, 0.2, 0.4, 1$  (top to bottom among the ones not specifically labelled, i.e.  $\lambda = 2, 5, 10$ ),  $Ca = 0.4$  and  $D/H = 0.6$ . The solid lines are for deformation along channel height,  $D_{T,y} = \Delta x/\Delta y$ , and the short-dashed lines for deformation along channel width,  $D_{T,z} = \Delta x/\Delta z$ .

viscosity ratio in the curves for steady-state drop deformation versus aspect ratio, as seen in figure 22(b), which is weaker than the effect of change in  $Ca$  (figure 22a). This difference is because the effect of change in  $\lambda$  on drop deformation is significant only for large drops at high capillary numbers, as seen previously in figure 9(b). It is interesting to note that there is a rapid decrease in drop deformation, both  $D_{T,y}$  and  $D_{T,z}$ , with a slight increase in aspect ratio from a square channel. This decrease shows that the effect of wall interactions is more important when the drop surface is in close vicinity to the wall and decays rapidly with distance. Furthermore, this sudden decrease in wall interactions must be responsible for the slight increase in drop steady-state velocity with a small deviation from a square cross-section, such that the reduced wall interaction has a dominant effect over the lower maximum centreline velocity of the channel, as observed in figures 21(a) and 21(b).

The simulations performed with varying aspect ratios for figures 21 and 22 are normalised by the channel average velocity ( $U_{av}$ ) for different aspect ratios but naturally have a varying maximum background velocity at the channel centreline ( $U_{max}$ ). Therefore, in figure 23, the effect of aspect ratio on drop steady-state velocity normalised by the maximum background velocity ( $U_{max}$ ) at the channel centreline from the Boussinesq (1868) solution is shown. Upon normalising by  $U_{max}$ , all the drop velocities for these conditions become less than unity and the variation in  $U_s/U_{max}$  is small (less than 10 %). The effect of decreasing  $U_{max}$  with increasing aspect ratio on the drop velocity is eliminated by this normalisation, thus isolating the effect of wall interactions. Therefore, we see in figure 23 that  $U_s/U_{max}$  first increases with increasing aspect ratio up to approximately  $W/H = 2.5$  due to a reduction in viscous interaction with the walls and then approaches the asymptote since the sidewalls are then far enough for their effect to be insignificant. The initial increase in  $U_s/U_{max}$  with changing aspect ratio can be linked with the sudden decrease in deformation upon deviation from a square cross-section observed in figure 22, confirming that the increase in  $U_s/U_{max}$  is due to reduced wall interactions.

Figure 24(a) compares numerical and experimental results for the effect of aspect ratio on the drop steady-state velocity. Experiments were conducted for a square channel and a rectangular channel with an aspect ratio of 2 : 1 with drops of  $D/H < 1$ . In the case of a square channel, an excellent match is observed, where the theory and experiments agree within 2 %–3 % for all values of  $D/H$ , whereas for the 2 : 1 rectangular channel, there

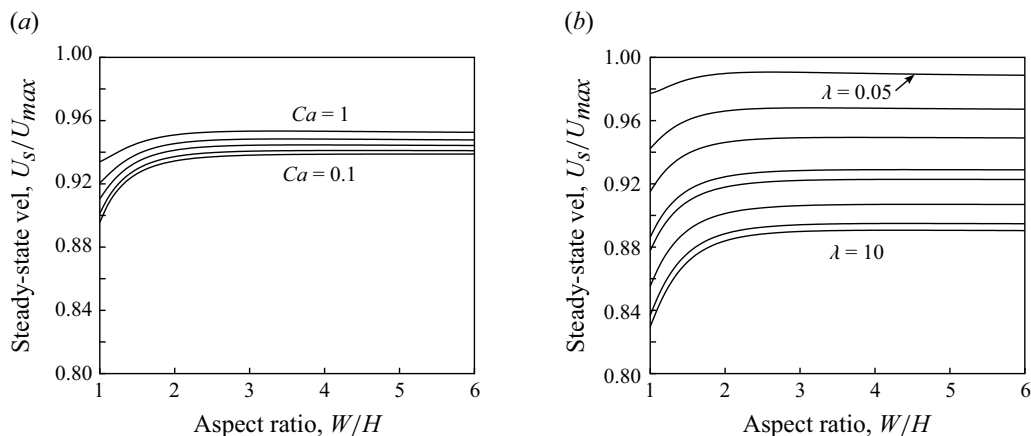


Figure 23. Steady-state drop velocity non-dimensionalised by maximum channel velocity with increasing aspect ratio for (a)  $Ca = 0.1, 0.3, 0.5, 0.7, 1.0$  (bottom to top),  $\lambda = 0.5$  and  $D/H = 0.6$  and (b)  $\lambda = 0.05, 0.2, 0.4, 0.8, 1, 2, 5, 10$  (top to bottom),  $Ca = 0.4$  and  $D/H = 0.6$ .

is a qualitative similarity between experiments and simulations, but the experimental data points are approximately 3%–8% below the simulation results for all but the smallest drop size. Simulation curves are also provided for larger aspect ratios up to a channel of infinite depth. The results for the channel of infinite depth were generated using the algorithm of Navarro *et al.* (2020). Convergence to the infinite-depth case with increasing  $W/H$  is slow, due to the stagnant zones near the corners. The steady-state velocities for drops suspended in an infinite-depth channel are very close to the limit  $U_{max}/U_{av} = 1.5$  for  $D/H \lesssim 0.5$  and then gradually increase with drop size (due to very low  $\lambda$  and high  $Ca$ ). Interestingly, it is observed that the steady-state drop velocities reach a plateau with increasing drop size for a square channel ( $W/H = 1$ ), but in the cases for channels with rectangular cross-section we see a monotonic increase in steady-state velocities with increasing drop size.

In figure 24(b), the same simulation results as figure 24(a) are shown but normalised by the maximum velocity of the background flow ( $U_{max}$ ) instead of the average velocity ( $U_{av}$ ). This simple modification nearly collapses all the curves, showing weak dependence of  $U_s/U_{max}$  on aspect ratio for drops with  $D/H \lesssim 1$ . In the case of a square channel ( $W/H = 1$ ) and a rectangular channel with  $W/H = 2$ , we observe a substantial difference in steady-state velocities for large drops ( $D/H \gtrsim 1$ ) when compared with the channels with larger aspect ratios. This is because wall interactions have a greater impact on steady-state drop velocities for large drops in narrower confinements. Therefore, even though the effect of  $U_{max}$  is nullified upon normalisation, the wall effects are highlighted at  $D/H \gtrsim 1$ , showing a lower steady-state velocity for narrower confinements. For the higher aspect ratios, we see a similar behaviour for  $U_s/U_{max}$  as in figure 23, where the steady-state velocities asymptote to a fixed value for  $W/H \gtrsim 2$ . Figure 24(b) also shows good agreement between the steady-state velocity of a drop with large viscosity ( $\lambda = 50$ ) and very small capillary numbers ( $Ca = 0.01, 0.1$ ) in a channel of  $W/H = 10$  obtained using the numerical framework of the current paper and the velocities of a solid sphere in a Poiseuille flow between plane parallel walls obtained by Staben *et al.* (2003) using BI simulations that have also been previously validated with experiments by Staben & Davis (2005).

For  $W/H = 2$  in figures 24(a) and 24(b), a drop of size  $D/H = 0.92$  was found to form two small satellite drops, leading to pinch-off, as shown in figure 24(c) along with

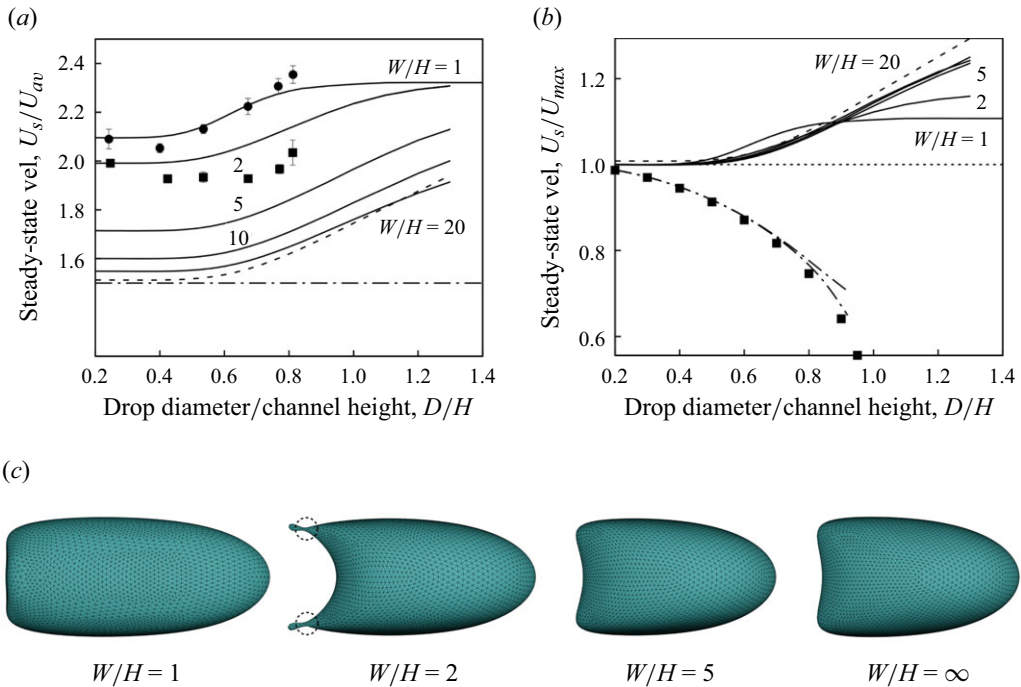


Figure 24. (a) Comparison between numerical and experimental results for steady-state drop velocity with increasing drop diameter at  $\lambda = 0.001$  (aqueous glycerol drop),  $Ca = 0.74$  and two aspect ratios. The solid theory curves are for increasing aspect ratios, with  $W/H = 1, 2, 5, 10, 20$  (top to bottom). The dot-dashed line is at  $U_s/U_{av} = 1.5$  to show the ratio  $U_{max}/U_{av} = 1.5$  for a plane Poiseuille flow. The short-dashed line shows the results for an infinite-depth straight channel using the algorithm of Navarro *et al.* (2020). The circle (●) and square (■) points are experimental results for a square channel and a rectangular channel of 2:1 aspect ratio respectively, with the error bars representing 90% confidence intervals. (b) The solid lines show steady-state drop velocity non-dimensionalised by maximum channel velocity with increasing drop radius for  $W/H = 1, 2, 5, 10, 20$  (bottom to top on the right end of the curves),  $Ca = 0.74$  and  $\lambda = 0.001$ . The dashed line is for a channel of infinite depth using the algorithm of Navarro *et al.* (2020) for the same conditions, and the dotted line shows  $U_{max}/U_{av} = 1.0$ . The dot-dashed line is for  $\lambda = 50$ ,  $Ca = 0.01$  and  $0.1$  (bottom to top),  $W/H = 10$  and the points (■) are simulations for a solid sphere between plane parallel walls from Staben *et al.* (2003). (c) Steady-state drop shapes obtained from BI simulations at  $\lambda = 0.001$ ,  $Ca = 0.74$ , and  $D/H = 0.92$  for  $W/H = 1, 5, \infty$ . At  $W/H = 2$  drop breaks off tails (dashed circles) before reaching steady state when started as a sphere.

the steady-state drop shapes for a drop of size  $D/H = 0.92$  at  $Ca = 0.74$ ,  $\lambda = 0.001$  and  $W/H = 1, 5$ , and  $\infty$ . However, when the drop ( $W/H = 2$ ,  $D/H = 0.92$ ) was started as a prolate ellipsoid instead of a sphere, the simulation could be continued until the drop reached a steady state. Note that in figures 24(a) and 24(b) the curves for  $W/H > 1$  are discontinued at  $D/H = 1.3$ . This is because we observed drop breakup due to a small satellite droplet formation (figure 25) at  $D/H = 1.4$ . Drops with  $D/H \geq 1$  are initially started as a prolate ellipsoid with a minor axis of  $0.4H$ , and the satellite drop breakup at  $D/H = 1.4$  occurs while the drop tries to relax from its initial highly deformed prolate ellipsoid shape. A prolate ellipsoid was used to keep a consistent initial shape with the narrower confinements ( $W/H = 1, 2$ ) where an oblate ellipsoid would not fit. It is possible that using an oblate ellipsoid could help avert such drop breakup.

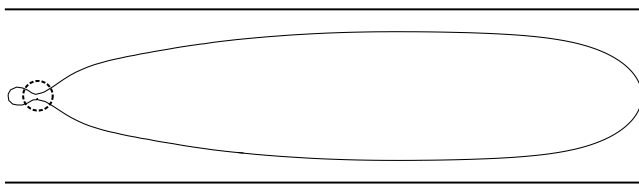


Figure 25. Satellite drop breakup at  $D/H = 1.4$  for  $W/H = 2$ ,  $\lambda = 0.001$ ,  $Ca = 0.74$ .

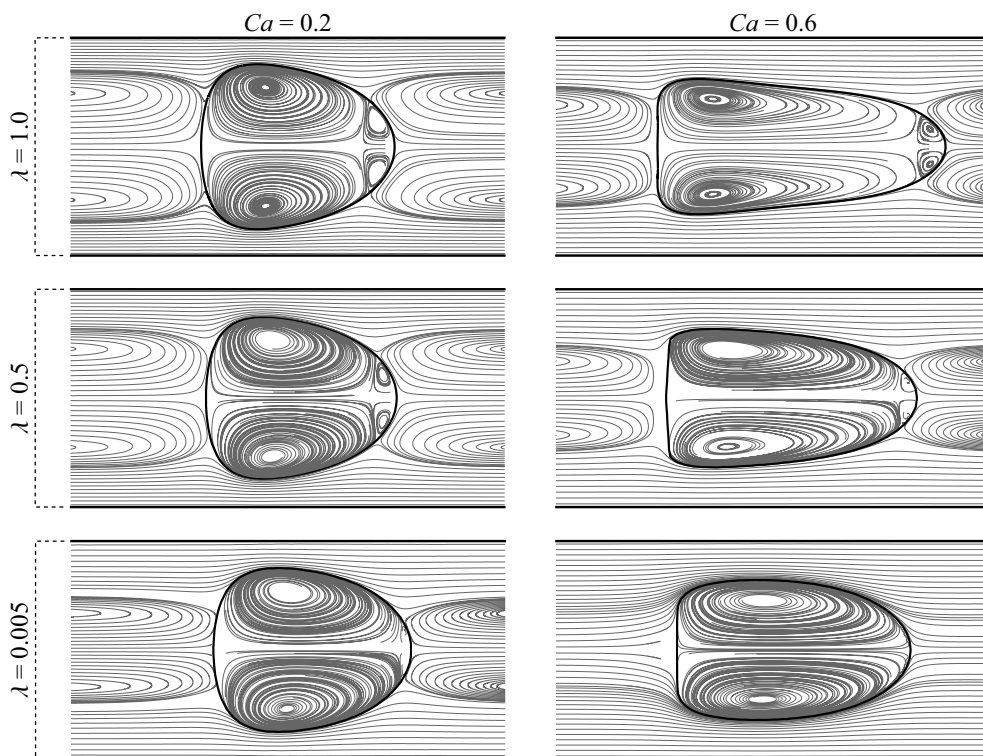


Figure 26. Streamlines showing the flow patterns in the  $x$ - $y$  plane containing the channel centreline, both inside and outside a drop of  $D/H = 0.8$  at  $\lambda = 1, 0.5, 0.05$  (top to bottom) and  $Ca = 0.2, 0.6$  (left to right) translating at steady state inside a straight channel of square cross-section.

#### 4.4. Velocity fields

Besides influencing droplet velocity and deformation, changes in capillary number and viscosity ratio may also lead to differences in the flow behaviour inside droplets, which plays an important role in applications such as microfluidic mixers (Stone & Stone 2005; Wang *et al.* 2015; Fu *et al.* 2018; Li *et al.* 2023). To illustrate the effect of these parameters on the flow inside and outside the droplet, figure 26 shows streamlines for a steady-state drop in a square channel for different viscosity ratios and capillary numbers in a cross-sectional  $x$ - $y$  plane at  $z = 0$ . The velocities outside the droplet were obtained from the BI representation of the velocity field outside the droplet:

$$\begin{aligned} \mathbf{u}(\mathbf{y}) = & \mathbf{u}_\infty(\mathbf{y}) + 2 \int_{S_\infty} \mathbf{n}(\mathbf{x}) \cdot \boldsymbol{\tau}(\mathbf{x} - \mathbf{y}) \cdot \mathbf{q}(\mathbf{x}) \, dS_x \\ & + \mathbf{F}(\mathbf{y}) + (\lambda - 1) \int_{S_d} \mathbf{n}(\mathbf{x}) \cdot \boldsymbol{\tau}(\mathbf{x} - \mathbf{y}) \cdot \mathbf{u}(\mathbf{x}) \, dS_x, \end{aligned} \quad (4.3)$$

where  $F(\mathbf{y})$  is given by (2.3). A detailed derivation can be found in Roure *et al.* (2023). In contrast, to calculate the flow velocity inside the drop, we solved a generalised BI equation, similar to previous works by Gissinger *et al.* (2021a) and Roure *et al.* (2023), using the velocity boundary conditions obtained from the numerical solution of (2.1)–(2.3). As in previous works (Martinez & Udell 1990; Lac & Sherwood 2009; Jing *et al.* 2024), the flow fields are calculated in the droplet frame of reference.

For  $\lambda = 1$ , and  $\lambda = 0.5$ , our results show flow patterns with small recirculation zones in the front portion of the drop, whereas larger recirculation zones are observed in the middle portion of the drop, similar to previous works (Martinez & Udell 1990; Lac & Sherwood 2009; Jing *et al.* 2024). The presence of the double-vortex structure in the external flow also indicates the existence of small recirculation regions in the back portion of the droplet, as reported by Martinez & Udell (1990) and Lac & Sherwood (2009), which are not captured in this resolution. As the droplet velocity increases (i.e. for higher  $Ca$  and smaller  $\lambda$ ), the external vortices, as well as the small vortex structures inside the droplet, decrease in size. For  $\lambda = 0.05$  and  $Ca = 0.6$ , as the drop steady-state velocity surpasses the maximum velocity of the background flow, the external vortices are no longer present and the smaller recirculation zones inside the droplet completely vanish.

The fluid flow in a rectangular channel is not axisymmetric. When a drop is pushed through a rectangular channel by a pressure-driven flow, there is larger space between the drop surface and the channel walls in the corner region than near the middle of the walls, so that the surrounding fluid is expected to flow with less resistance near the channel corners. To investigate this corner flow, we plotted the velocity fields of the surrounding liquid flow in a  $y$ - $z$  cross-sectional plane of a square channel ( $y \in [0, 1]$  and  $z \in [-0.5, 0.5]$ ) at a position halfway between the drop nose and its centroid in figures 27(a)–(c) for  $\lambda = 0.05$ ,  $Ca = 0.1$ , and different drop sizes. The observations indicate that the flow is directed into the channel corner from the middle of the walls, verifying this expectation. This flow pattern differs from what is typically observed in axisymmetric channels and is most prominent in drops at low  $Ca$  and low  $\lambda$ . Figure 27(d) shows the velocity vectors of the surrounding fluid flow for a drop of  $D/H = 0.6$ ,  $\lambda = 0.05$ , and  $Ca = 0.1$  in a  $y$ - $z$  cross-sectional plane at the nose of the drop. We have previously observed the presence of recirculation vortices in the bulk fluid flow pattern outside the drop in figure 26. These recirculation vortices are usually larger for drops of bigger size. Therefore, we see that the velocity fields in a cross-sectional  $y$ - $z$  plane at the nose of the drop changes direction close to the channel centreline in figure 27(d). Away from the centreline, there is a weak flow to the corner regions. On the rear half of the drop (not shown), the flow in the  $y$ - $z$  cross-sectional plane is away from the corners.

Figure 28 shows the velocity vectors of the surrounding fluid flow for a drop of  $D/H = 0.8$ ,  $\lambda = 0.05$ , and  $Ca = 0.1$  in (a) the  $x$ - $y$  plane and (b) the  $x$ - $y'$  plane, where  $y'$  is the diagonal of the square cross-section of the microchannel, starting at one corner. The flow pattern outside the drop in the plane containing this diagonal (figure 28b) is qualitatively similar to that in the  $x$ - $y$  plane (figure 28a), except that there is more space between the drop surface and the walls. Hence, the flow is stronger in the corner regions and the recirculation vortices are smaller in the diagonal plane than the  $x$ - $y$  plane.

## 5. Conclusions

The dynamics of a 3-D deformable drop in a straight channel of rectangular cross-section was studied both experimentally and numerically in this work. A novel MFBI algorithm developed by Roure *et al.* (2023) was adapted here to generate the numerical results. This particular case of simulating straight channels does not require a separate

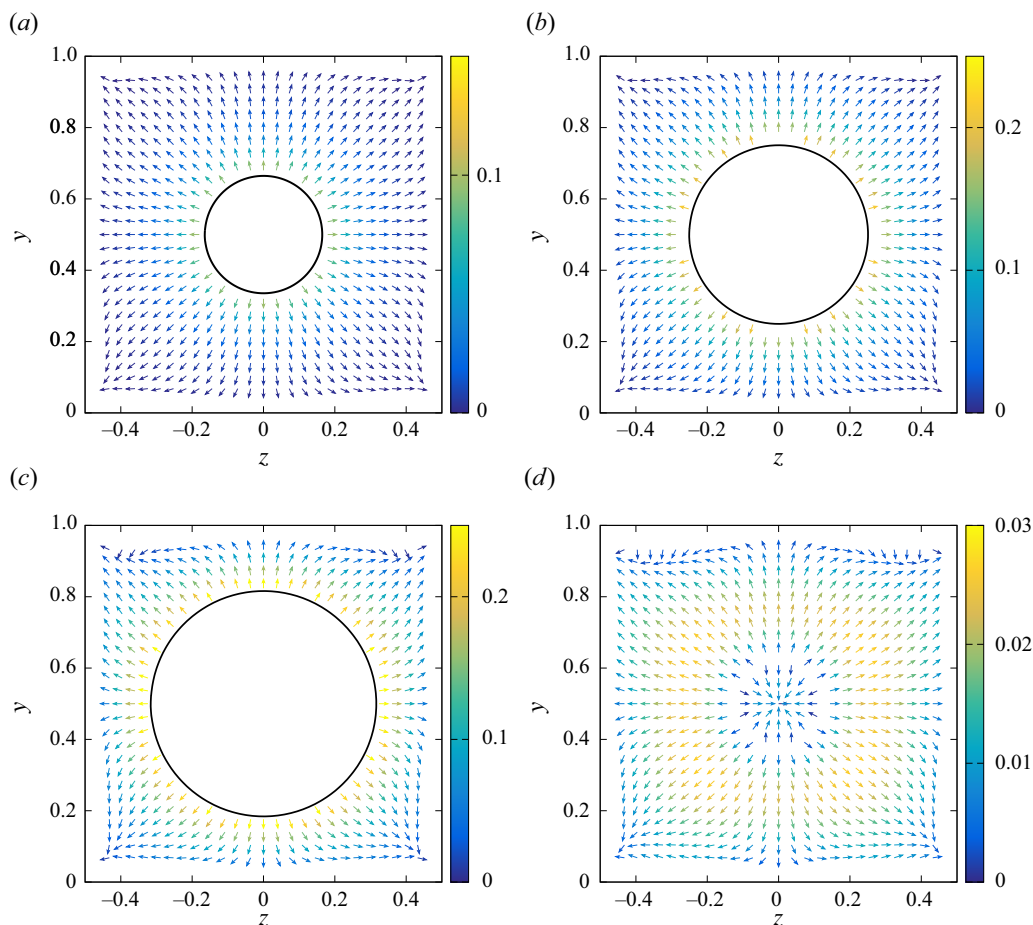


Figure 27. Velocity fields of the surrounding fluid flow in a  $y$ - $z$  cross-sectional plane midway between the drop nose and drop centroid for  $\lambda = 0.05$ ,  $Ca = 0.1$ , and (a)  $D/H = 0.4$ , (b)  $D/H = 0.6$  and (c)  $D/H = 0.8$ ; (d)  $y$ - $z$  cross-sectional plane at the nose of a drop for same conditions as (b). The solid curves show the drop contours in (a), (b) and (c).

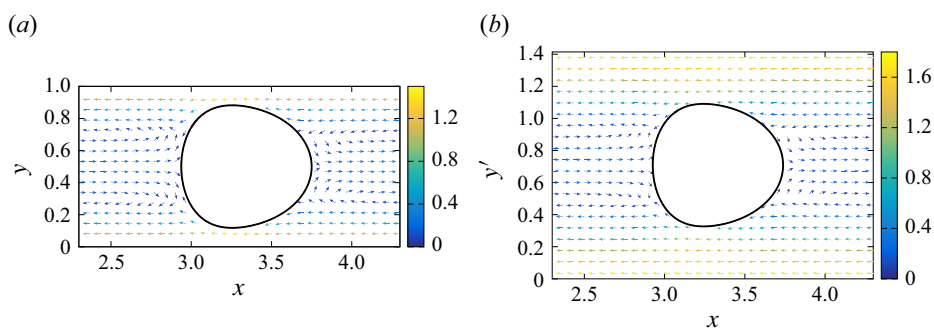


Figure 28. Velocity fields of the surrounding fluid flow for a drop of  $\lambda = 0.05$ ,  $Ca = 0.1$ , and  $D/H = 0.8$  in (a) the  $x$ - $y$  plane and (b)  $x$ - $y'$  plane, where  $y'$  is the diagonal of the square cross-section of the channel. The solid curves show the drop contours.

solution for the background flow using BI equations, since we can directly impose the Boussinesq (1868) flow profile. The hydrodynamic contributions from the walls to the drop and *vice versa* are calculated within this MF rather than the whole domain, reducing the computational cost of the simulations. Direct comparison was done between the BI algorithm used in the current work with the spectral-boundary-element method used by Wang & Dimitrakopoulos (2012), with a good agreement between the two for the limited cases in common. Experiments were performed in a macroscopic flow cell constructed for easy drop visualisation using a high-viscosity fluid as the suspending medium to ensure a low Reynolds number. An insert allows the ability to easily change channel aspect ratios. ImageJ was used to analyse the drop videos to extract data such as deformation and steady-state velocity. Both experiments and simulations were run over a variety of conditions.

We investigated the effect of change in drop size, drop-to-bulk viscosity ratio, capillary number and channel aspect ratio on the kinematics of the drop and its deformed shape. A drop released in a background flow always reaches a steady state below a critical capillary number. The general trend observed in both experiments and simulations is that the steady-state velocity of the drop decreases with increasing viscosity ratio due to greater hydrodynamical resistance to flow and increases with increasing capillary number owing to the higher deformation at high  $Ca$  that keeps the drop closer to the channel maximum velocity at the centreline and away from the walls. The effect of viscosity ratio on steady-state drop deformation was seen to be significant only for large drops at high capillary numbers. In general, the steady-state velocity of a drop decreases with increasing drop diameter due to increased interaction with the walls, except for cases with low viscosity ratios and high capillary numbers. A low-viscosity drop of sufficiently large size and deformability was also found to move faster than the maximum velocity of the background flow, similar to the findings of Lac & Sherwood (2009) for a large drop in a cylindrical tube.

Upon increasing the channel aspect ratio from a square channel, keeping the average flow velocity ( $U_{av}$ ) constant, the steady-state velocity of a drop was found to increase first up to an aspect ratio of 1.3 due to decreased wall interactions, and then decrease monotonically due to the decrease in  $U_{max}$ . Upon normalising the drop velocity by  $U_{max}$ , we eliminate the effect of decreasing maximum flow velocity with increasing aspect ratio and observe an increase in drop velocity with increasing aspect ratio due to reduced wall interactions, eventually asymptoting to a constant value when the walls are too far away to have a noticeable contribution. Comparisons of our finite-depth channel simulations were done with the infinite-depth simulation algorithm of Navarro *et al.* (2020), where we see faster convergence between the two when the drop velocities are normalised by  $U_{max}$  rather than  $U_{av}$ .

We also studied the cross-stream migration of drops that start away from the channel centreline. For cases with drop size comparable to channel height, the drop migrates towards the channel centreline. A drop experiences a spike in the lateral migration velocity immediately upon release, due to the initial deformation. Then the drop develops a tail due to wall interactions, but eventually becomes compact and reaches a steady shape at the channel centreline. The dynamics of this lateral migration was also found to depend on the drop-to-bulk viscosity ratio and the capillary number. A low-viscosity drop migrates faster owing to the lower hydrodynamical resistance and the rapid initial deformation experienced by it. In general, a drop with a higher capillary number was found to migrate to the channel centreline the earliest, since it experiences a higher deformation and maintains a deformed shape for longer, although some non-monotonic behaviour was observed in stages before reaching the centreline.

The interesting behaviour at low viscosity ratios motivates us to do further research on such conditions. In a future work, we will extend the BI algorithm to study the effect of

surfactants on the steady-state dynamics of low-viscosity drops. We expect the reduced interfacial mobility due to the presence of surfactants and the associated Marangoni stresses to be highlighted at low viscosity ratios, resulting in much-retarded steady-state velocities compared with clean drops.

**Acknowledgements.** The authors thank D. Mejjic for assistance with the design and fabrication of the channel used in the experiments.

**Funding.** This work was funded, in part, by award no. 2301910 from the US National Science Foundation. The undergraduate assistants (A.S. and A.V.) received support from the University of Colorado's Undergraduate Research Opportunities Program, Biological Sciences Initiative and Summer Program for Undergraduate Research.

**Declaration of interests.** The authors report no conflict of interest.

**Author contributions.** R.C. performed the numerical simulations, wrote the manuscript, and worked with undergraduate students on the experiments; G.R. developed the code for the simulations, worked with undergraduate students on the experiments and edited the manuscript; A.S. and A.V. participated in the design, implementation and analysis of experiments; R.D. supervised the students and project, secured funding and edited the manuscript.

#### REFERENCES

- ANNA, S.L. 2016 Droplets and bubbles in microfluidic devices. *Annu. Rev. Fluid Mech.* **48** (2016), 285–309.
- ATASI, O., HAUT, B., PEDRONO, A., SCHEID, B. & LEGENDRE, D. 2018 Influence of soluble surfactants and deformation on the dynamics of centered bubbles in cylindrical microchannels. *Langmuir* **34** (34), 10048–10062.
- AUTEBERT, J., COUDERT, B., BIDARD, F., PIERGA, J., DESCROIX, S., MALAQUIN, L. & VIOVY, J. 2012 Microfluidic: an innovative tool for efficient cell sorting. *Methods* **57** (3), 297–307.
- BAROUD, C.N., GALLAIRE, F. & DANGLA, R. 2010 Dynamics of microfluidic droplets. *Lab Chip* **10** (16), 2032–2045.
- BOUSSINESQ, J. 1868 Mémoire sur l'influence des frottements dans les mouvements réguliers des fluids. *Journal de Mathématiques Pures et Appliquées* **13** (2), 377–424.
- BRETHERTON, F.P. 1961 The motion of long bubbles in tubes. *J. Fluid Mech.* **10** (2), 166–188.
- CAPPELLO, J., RIVERO-RODRÍGUEZ, J., VITRY, Y., DEWANDRE, A., SOBAC, B. & SCHEID, B. 2023 Beads, bubbles and drops in microchannels: stability of centred position and equilibrium velocity. *J. Fluid Mech.* **956**, A21.
- CHAN, P.C.H. & LEAL, L.G. 1979 The motion of a deformable drop in a second-order fluid. *J. Fluid Mech.* **92** (1), 131–170.
- CHEN, Y. & DENG, Z. 2017 Hydrodynamics of a droplet passing through a microfluidic T-junction. *J. Fluid Mech.* **819**, 401–434.
- CHERLO, S.K.R., KARIVETI, S. & PUSHPAVANAM, S. 2010 Experimental and numerical investigations of two-phase flow behavior in rectangular microchannels. *Ind. Engng Chem. Res.* **49** (2), 893–899.
- COULLIETTE, C. & POZRIKIDIS, C. 1998 Motion of an array of drops through a cylindrical tube. *J. Fluid Mech.* **358**, 1–28.
- DE MENECH, M., GARSTECKI, P., JOUSSE, F. & STONE, H.A. 2008 Transition from squeezing to dripping in a microfluidic T-shaped junction. *J. Fluid Mech.* **595**, 141–161.
- DING, Y., HOWES, P.D. & DEMELLO, A.J. 2020 Recent advances in droplet microfluidics. *Anal. Chem.* **92** (1), 132–149.
- FU, Y., BAI, L., ZHAO, S., ZHANG, X., JIN, Y. & CHENG, Y. 2018 Simulation of reactive mixing behaviors inside micro-droplets by a lattice Boltzmann method. *Chem. Engng Sci.* **181**, 79–89.
- GISSINGER, J.R., ZINCHENKO, A.Z. & DAVIS, R.H. 2021a Internal circulation and mixing within tight-squeezing deformable droplets. *Phys. Rev. E* **103** (4), 043106.
- GISSINGER, J.R., ZINCHENKO, A.Z. & DAVIS, R.H. 2021b Drop squeezing between arbitrary smooth obstacles. *J. Fluid Mech.* **908**, A33.
- GREENSTEIN, T. & HAPPEL, J. 1968 Theoretical study of the slow motion of a sphere and a fluid in a cylindrical tube. *J. Fluid Mech.* **34** (4), 705–710.
- GRIGGS, A.J., ZINCHENKO, A.Z. & DAVIS, R.H. 2007 Low-Reynolds-number motion of a deformable drop between two parallel plane walls. *Intl J. Multiphase Flow* **33** (2), 182–206.

- HADIKHANI, P., HASHEMI, S.M.H., BALESTRA, G., ZHU, L., MODESTINO, M.A., GALLAIRE, F. & PSALTIS, D. 2018 Inertial manipulation of bubbles in rectangular microfluidic channels. *Lab Chip* **18** (7), 1035–1046.
- HAPPEL, J. & BRENNER, H. 1983 *Low Reynolds Number Hydrodynamics: with Special Applications to Particulate Media*, pp. 286–357. Springer.
- HELMERS, T., KEMPER, P., THÖMING, J. & MIESSNER, U. 2019a Modeling the excess velocity of low-viscous Taylor droplets in square microchannels. *Fluids* **4** (3), 162.
- HELMERS, T., KEMPER, P., THÖMING, J. & MIESSNER, U. 2019b Determining the flow-related cap deformation of Taylor droplets at low ca numbers using ensemble-averaged high-speed images. *Exp. Fluids* **60** (7), 1–17.
- HETSRONI, G., HABER, S. & WACHOLDER, E. 1970 The flow fields in and around a droplet moving axially within a tube. *J. Fluid Mech.* **41** (4), 689–705.
- HO, B.P. & LEAL, L.G. 1975 The creeping motion of liquid drops through a circular tube of comparable diameter. *J. Fluid Mech.* **71** (2), 361–383.
- HOANG, D.A., VAN STEIJN, V., PORTELA, L.M., KREUTZER, M.T. & KLEIJN, C.R. 2013a Benchmark numerical simulations of segmented two-phase flows in microchannels using the volume of fluid method. *Comput. Fluids* **86**, 28–36.
- HOANG, D.A., PORTELA, L.M., KLEIJN, C.R., KREUTZER, M.T. & VAN STEIJN, V. 2013b Dynamics of droplet breakup in a T-junction. *J. Fluid Mech.* **717**, R4.
- HODGES, S.R., JENSEN, O.E. & RALLISON, J.M. 2004 The motion of a viscous drop through a cylindrical tube. *J. Fluid Mech.* **501**, 279–301.
- HORWITZ, J.A.K., KUMAR, P. & VANKA, S.P. 2014 Three-dimensional deformation of a spherical droplet in a square duct flow at moderate Reynolds numbers. *Intl J. Multiphase Flow* **67**, 10–24.
- HUR, S.C., HENDERSON-MACLENNAN, N.K., MCCABE, E.R.B. & DI CARLO, D. 2011 Deformability-based cell classification and enrichment using inertial microfluidics. *Lab Chip* **11** (5), 912–920.
- JAKIELA, S. 2016 Measurement of the hydrodynamic resistance of microdroplets. *Lab Chip* **16** (19), 3695–3699.
- JAKIELA, S., MAKULSKA, S., KORCZYK, P.M. & GARSTECKI, P. 2011 Speed of flow of individual droplets in microfluidic channels as a function of the capillary number, volume of droplets and contrast of viscosities. *Lab Chip* **11** (21), 3603–3608.
- JANSSEN, P.J.A. & ANDERSON, P.D. 2007 Boundary-integral method for drop deformation between parallel plates. *Phys. Fluids* **19** (4), 043602.
- JING, D., LU, R., FARUTIN, A., GUO, Z., WANG, F., WANG, W., MISBAH, C. & SUI, Y. 2024 Droplets can enhance microcapsule deformation in channel flow. *Commun. Phys.* **7** (1), 310.
- JOVANOVIĆ, J., ZHOU, W., REBROV, E.V., NIJHUIS, T.A., HESSEL, V. & SCHOUTEN, J.C. 2011 Liquid–liquid slug flow: Hydrodynamics and pressure drop. *Chem. Engng Sci.* **66** (1), 42–54.
- KADIVAR, E. 2018 Modeling droplet deformation through converging–diverging microchannels at low Reynolds number. *Acta Mech.* **229** (10), 4239–4250.
- KHAN, M.A. & WANG, Y. 2010 Droplet motion in a microconfined shear flow via a three-dimensional spectral boundary element method. *Phys. Fluids* **22** (12), 123301.
- KHAYAT, R.E., LUCIANI, A. & UTRACKI, L.A. 1997 Boundary-element analysis of planar drop deformation in confined flow. Part 1. Newtonian fluids. *Engng Anal. Bound. Elem.* **19** (4), 279–289.
- KINOSHITA, H., KANEDA, S., FUJII, T. & OSHIMA, M. 2007 Three-dimensional measurement and visualization of internal flow of a moving droplet using confocal micro-PIV. *Lab Chip* **7** (3), 338–346.
- LAC, E. & SHERWOOD, J.D. 2009 Motion of a drop along the centreline of a capillary in a pressure-driven flow. *J. Fluid Mech.* **640**, 27–54.
- LAN, H. & KHISMATULLIN, D.B. 2012 A numerical study of the lateral migration and deformation of drops and leukocytes in a rectangular microchannel. *Intl J. Multiphase Flow* **47**, 73–84.
- LI, M., BOULAFENTIS, T., STATHOULOPOULOS, A., LIU, Z. & BALABANI, S. 2023 Flows inside polymer microfluidic droplets: role of elasticity. *Chem. Engng Sci.* **278**, 118887.
- LI, X., HE, L., HE, Y., GU, H. & LIU, M. 2019 Numerical study of droplet formation in the ordinary and modified T-junctions. *Phys. Fluids* **31** (8), 082101.
- LUO, Z.Y., SHANG, X.L. & BAI, B.F. 2018 Marangoni effect on the motion of a droplet covered with insoluble surfactant in a square microchannel. *Phys. Fluids* **30** (7), 077101.
- MARTINEZ, M.J. & UDELL, K.S. 1990 Axisymmetric creeping motion of drops through circular tubes. *J. Fluid Mech.* **210**, 565–591.
- MORTAZAVI, S. & TRYGGVASON, G. 2000 A numerical study of the motion of drops in Poiseuille flow. Part 1. Lateral migration of one drop. *J. Fluid Mech.* **411**, 325–350.
- NATH, B., BISWAS, G., DALAL, A. & SAHU, K.C. 2017 Migration of a droplet in a cylindrical tube in the creeping flow regime. *Phys. Rev. E* **95** (3), 033110.

- NAVARRO, R., MARISTANY, A. & DAVIS, R.H. 2021 Simulation of drop motion and breakup in narrow pores. *Chem. Engng Sci.* **229**, 116057.
- NAVARRO, R., ZINCHENKO, A.Z. & DAVIS, R.H. 2020 Boundary-integral study of a freely suspended drop in a T-shaped microchannel. *Intl J. Multiphase Flow* **130**, 103379.
- OLBRICHT, W.L. & KUNG, D.M. 1992 The deformation and breakup of liquid drops in low Reynolds number flow through a capillary. *Phys. Fluids A* **4** (7), 1347–1354.
- OLBRICHT, W.L. & LEAL, L.G. 1982 The creeping motion of liquid drops through a circular tube of comparable diameter: the effect of density differences between the fluids. *J. Fluid Mech.* **115** (1), 187–216.
- PAK, O.S., FENG, J. & STONE, H.A. 2014 Viscous Marangoni migration of a drop in a Poiseuille flow at low surface Péclet numbers. *J. Fluid Mech.* **753**, 535–552.
- RAJ, R., MATHUR, N. & BUWA, V.V. 2010 Numerical simulations of liquid-liquid flows in microchannels. *Ind. Engng Chem. Res.* **49** (21), 10606–10614.
- RALLISON, J.M. & ACRIVOS, A. 1978 A numerical study of the deformation and burst of a viscous drop in an extensional flow. *J. Fluid Mech.* **89** (1), 191–200.
- RAO, S.S. & WONG, H. 2018 The motion of long drops in rectangular microchannels at low capillary numbers. *J. Fluid Mech.* **852**, 60–104.
- RIVERO-RODRIGUEZ, J. & SCHEID, B. 2018 Bubble dynamics in microchannels: inertial and capillary migration forces. *J. Fluid Mech.* **842**, 215–247.
- ROURE, G., ZINCHENKO, A.Z. & DAVIS, R.H. 2024 Dynamics and active mixing of a droplet in a Stokes trap. *J. Fluid Mech.* **985**, A15.
- ROURE, G., ZINCHENKO, A.Z. & DAVIS, R.H. 2023 Numerical simulation of deformable droplets in three-dimensional, complex-shaped microchannels. *Phys. Fluids* **35** (10), 102013.
- SARRAZIN, F., BONOMETTI, T., PRAT, L., GOURDON, C. & MAGNAUDET, J. 2008 Hydrodynamic structures of droplets engineered in rectangular micro-channels. *Microfluid Nanofluid* **5** (1), 131–137.
- SHANG, L., CHENG, Y. & ZHAO, Y. 2017 Emerging droplet microfluidics. *Chem. Rev.* **117** (12), 7964–8040.
- SHAPIRA, M. & HABER, S. 1988 Low Reynolds number motion of a droplet between two parallel plates. *Intl J. Multiphase Flow* **14** (4), 483–506.
- SHEN, Y., YALIKUN, Y. & TANAKA, Y. 2019 Recent advances in microfluidic cell sorting systems. *Sensors Actuators B* **282**, 268–281.
- SHIELDS, C.W., IV, REYES, C.D. & LÓPEZ, G.P. 2015 Microfluidic cell sorting: a review of the advances in the separation of cells from debulking to rare cell isolation. *Lab Chip* **15** (5), 1230–1249.
- SIBILLO, V., PASQUARIELLO, G., SIMEONE, M., CRISTINI, V. & GUIDO, S. 2006 Drop deformation in microconfined shear flow. *Phys. Rev. Lett.* **97** (5), 054502.
- SINGLA, A., MEHUL, B. & RAY, B. 2024 Droplet dynamics in a constricted microchannel. *Chem. Engng Sci.* **300**, 120532.
- SONG, H., TICE, J.D. & ISMAGILOV, R.F. 2003 A microfluidic system for controlling reaction networks in time. *Angew. Chem. Intl Ed.* **42** (7), 768–772.
- STABEN, M.E. & DAVIS, R.H. 2005 Particle transport in Poiseuille flow in narrow channels. *Intl J. Multiphase Flow* **31** (5), 529–547.
- STABEN, M.E., ZINCHENKO, A.Z. & DAVIS, R.H. 2003 Motion of a particle between two parallel plane walls in low-Reynolds-number Poiseuille flow. *Phys. Fluids* **15** (6), 1711–1733.
- STONE, Z.B. & STONE, H.A. 2005 Imaging and quantifying mixing in a model droplet micromixer. *Phys. Fluids* **17** (6), 063103.
- TICE, J.D., SONG, H., LYON, A.D. & ISMAGILOV, R.F. 2003 Formation of droplets and mixing in multiphase microfluidics at low values of the Reynolds and the capillary numbers. *Langmuir* **19** (22), 9127–9133.
- UNVERDI, S.O. & TRYGGVASON, G. 1992 A front-tracking method for viscous, incompressible, multi-fluid flows. *J. Comput. Phys.* **100** (1), 25–37.
- VANANROYE, A., JANSSEN, P.J.A., ANDERSON, P.D., VAN PUYVELDE, P. & MOLDENAERS, P. 2008 Microconfined equiviscous droplet deformation: comparison of experimental and numerical results. *Phys. Fluids* **20** (1), 013101.
- VANAPALLI, S.A., BANPURKAR, A.G., VAN DEN ENDE, D., DUIJS, M.H.G. & MUGELE, F. 2009 Hydrodynamic resistance of single confined moving drops in rectangular microchannels. *Lab Chip* **9** (7), 982–990.
- WANG, J., WANG, J., FENG, L. & LIN, T. 2015 Fluid mixing in droplet-based microfluidics with a serpentine microchannel. *RSC Adv.* **5** (126), 104138–104144.
- WANG, Y. & DIMITRAKOPOULOS, P. 2012 Low-Reynolds-number droplet motion in a square microfluidic channel. *Theor. Comput. Fluid Dyn.* **26** (1–4), 361–379.
- WONG, H., RADKE, C.J. & MORRIS, S. 1995 The motion of long bubbles in polygonal capillaries. Part 2. Drag, fluid pressure and fluid flow. *J. Fluid Mech.* **292**, 95–110.

- XI, H. *et al.* 2017 Active droplet sorting in microfluidics: a review. *Lab Chip* **17** (5), 751–771.
- YONG, Y., YANG, C., JIANG, Y., JOSHI, A., SHI, Y. & YIN, X. 2011 Numerical simulation of immiscible liquid-liquid flow in microchannels using Lattice Boltzmann method. *Sci. China: Chem.* **54** (1), 244–256.
- ZADEH, S.S.S., EGAN, V. & WALSH, P. 2022 An experimental study on the mobility of droplets in liquid-liquid Taylor flows within circular capillaries. *Intl J. Multiphase Flow* **157**, 104259.
- ZHOU, H. & POZRIKIDIS, C. 1993a The flow of ordered and random suspensions of two-dimensional drops in a channel. *J. Fluid Mech.* **255** (-1), 103–127.
- ZHOU, H. & POZRIKIDIS, C. 1993b The flow of suspensions in channels: single files of drops. *Phys. Fluids A: Fluid Dyn.* **5** (2), 311–324.
- ZHOU, H. & POZRIKIDIS, C. 1994 Pressure-driven flow of suspensions of liquid drops. *Phys. Fluids* **6** (1), 80–94.
- ZINCHENKO, A.Z., ASHLEY, J.F. & DAVIS, R.H. 2012 A moving-frame boundary-integral method for particle transport in microchannels of complex shape. *Phys. Fluids* **24** (4), 043302.
- ZINCHENKO, A.Z. & DAVIS, R.H. 2000 An efficient algorithm for hydrodynamical interaction of many deformable drops. *J. Comput. Phys.* **157** (2), 539–587.
- ZINCHENKO, A.Z., ROTHER, M.A. & DAVIS, R.H. 1997 A novel boundary-integral algorithm for viscous interaction of deformable drops. *Phys. Fluids* **9** (6), 1493–1511.
- ZINCHENKO, A.Z., ROTHER, M.A. & DAVIS, R.H. 1999 Cusping, capture, and breakup of interacting drops by a curvatureless boundary-integral algorithm. *J. Fluid Mech.* **391**, 249–292.